Rainfall Teleconnections with Indo-Pacific Variability in the WCRP CMIP3 Models

WENJU CAI, ARNOLD SULLIVAN, AND TIM COWAN

CSIRO Marine and Atmospheric Research, Aspendale, Victoria, and Wealth from Oceans National Research Flagship, CSIRO, North Ryde, New South Wales, Australia

(Manuscript received 25 June 2008, in final form 30 March 2009)

ABSTRACT

The present study assesses the ability of climate models to simulate rainfall teleconnections with the El Niño–Southern Oscillation (ENSO) and the Indian Ocean dipole (IOD). An assessment is provided on 24 climate models that constitute phase 3 of the World Climate Research Programme's Coupled Model Intercomparison Project (WCRP CMIP3), used in the Fourth Assessment Report (AR4) of the Intergovernmental Panel on Climate Change (IPCC).

The strength of the ENSO–rainfall teleconnection, defined as the correlation between rainfall and Niño-3.4, is overwhelmingly controlled by the amplitude of ENSO signals relative to stochastic noise, highlighting the importance of realistically simulating this parameter. Because ENSO influences arise from the movement of convergence zones from their mean positions, the well-known equatorial Pacific climatological sea surface temperature (SST) and ENSO cold tongue anomaly biases lead to systematic errors. The climatological SSTs, which are far too cold along the Pacific equator, lead to a complete ''nonresponse to ENSO'' along the central and/or eastern equatorial Pacific in the majority of models. ENSO anomalies are also too equatorially confined and extend too far west, with linkages to a weakness in the teleconnection with Hawaii boreal winter rainfall and an inducement of a teleconnection with rainfall over west Papua New Guinea in austral summer. Another consequence of the ENSO cold tongue bias is that the majority of models produce too strong a coherence between SST anomalies in the west, central, and eastern equatorial Pacific. Consequently, the models' ability in terms of producing differences in the impacts by ENSO from those by ENSO Modoki is reduced.

Similarly, the IOD–rainfall teleconnection strengthens with an intensification of the IOD relative to the stochastic noise. A significant relationship exists between intermodel variations of IOD–ENSO coherence and intermodel variations of the ENSO amplitude in a small subset of models in which the ENSO anomaly structure and ENSO signal transmission to the Indian Ocean are better simulated. However, using all but one model (defined as an outlier) there is no systematic linkage between ENSO amplitude and IOD–ENSO coherence. Indeed, the majority of models produce an ENSO–IOD coherence lower than the observed, supporting the notion that the Indian Ocean has the ability to generate independent variability and that ENSO is not the only trigger of the IOD. Although models with a stronger IOD amplitude and rainfall teleconnection tend to have a greater ENSO amplitude, there is no causal relationship; instead this feature reflects a commensurate strength of the Bjerknes feedback in both the Indian and Pacific Oceans.

1. Introduction

The simulations with contemporary coupled general circulation models (GCMs) conducted recently as a part of phase 3 of the World Climate Research Programme's Coupled Model Intercomparison Project (WCRP CMIP3) for the Fourth Assessment Report (AR4) of the Intergovernmental Panel on Climate Change (IPCC) provide an opportunity for a comprehensive examination of the impacts of climate variability in the Indo-Pacific system on global rainfall. Recent analysis of these integrations has shown that there have been significant improvements in GCMs simulating El Niño–Southern Oscillation (ENSO) (AchutaRao and Sperber 2002; Joseph and Nigam 2006; Guilyardi 2006). It has also been shown that the majority of models produce an equatorial zonal mode with spatial structures and seasonality similar to the observed Indian Ocean dipole (IOD) (Saji et al. 1999; Webster et al. 1999; Murtugudde et al. 2000), with a realistic interplay between the thermocline depth, sea surface temperature (SST), precipitation, and zonal winds (Saji et al. 2006). It is less clear how these models

Corresponding author address: Dr. Wenju Cai, 107-121 Station St., Aspendale, VIC 3195, Australia.
E-mail: wenju.cai@csiro.au

DOI: 10.1175/2009JCLI2694.1

perform in terms of a rainfall teleconnection with these modes of variability, despite a recent focus on the ENSO–monsoon relationship (e.g., Ashrit et al. 2003; Turner et al. 2005; Annamalai et al. 2007) and the ENSO–rainfall teleconnection to tropical rainfall in some CMIP3 models (Joseph and Nigam 2006). As will be clear, the ENSO–rainfall and IOD–rainfall teleconnections vary vastly from model to model. We will focus on factors controlling the intermodel variations.

ENSO affects rainfall over many parts of the globe (Philander 1990; Ropelewski and Halpert 1987, 1989; van Loon and Shea 1985; Shukla and Paolino 1983; McBride and Nicholls 1983). During El Niño, cooling in the west Pacific and warming in the central and eastern equatorial Pacific lead to more uniform SSTs. In association, a merger of the major convergence zones occurs: the intertropical convergence zone (ITCZ) moves equatorward, while the South Pacific convergence zone (SPCZ) shifts northward, and the convergence zone over the west Pacific migrates to the east, where warm SST anomalies develop. The merger of these convective zones generates heavy rainfall in the central and eastern Pacific and droughts in the west encompassing Indonesia, the Philippines, Hawaii, eastern Australia, and the Fijian Islands. The equatorward displacement of the ITCZ brings heavy rainfall to equatorial regions such as Ecuador but drought further north, particularly around Central America. In the Indian Ocean sector, boreal summer monsoons tend to fail and southeastern Africa often suffers drought, while Sri Lanka and equatorial East Africa experience increased rainfall (Philander 1990).

Like ENSO, the IOD has been shown to affect rainfall in many countries on the Indian Ocean rim and beyond (Saji and Yamagata 2003a,b; Yamagata et al. 2004; Behera et al. 2005). In a similar way, the associated rainfall variability reflects the movement of the convergence zones in the Indian Ocean sector, which can superimpose or counteract the impacts of ENSO. The IOD has been shown to influence the interannual variability of the Indian summer monsoon rainfall (Ashok et al. 2001). They found that, whenever the ENSO–monsoon correlation is low, the IOD–monsoon correlation is high. Through changes in the Walker circulation and water vapor transport, a positive IOD (pIOD) event in austral winter and spring causes drought in Indonesia and Australia (Ashok et al. 2003; Cai et al. 2005) and flooding in eastern Africa (Behera et al. 2005; Black et al. 2003; Zubair et al. 2003).

As the convergence zones are directly linked with wind, sea level pressure, and SST anomalies, benchmarking a climate model in terms of a rainfall teleconnection is a synthetic assessment beyond rainfall itself. Furthermore, a major thrust of the CMIP3 process is to provide projections of a future climate. In an assessment of the likely future rainfall changes a number of studies have focused on whether the Pacific response to global warming is El Niño– or La Niña–like (Meehl and Washington 1996; Collins 2005; Timmermann et al. 1999; Cai and Whetton 2001; Vecchi et al. 2006; Lu et al. 2008) and if the Indian Ocean's response is pIOD-like (Shi et al. 2008b). Recent studies have shown that a projected Australia rainfall change is consistent with the response in modes of variability and their rainfall teleconnections (Cai and Cowan 2006; Shi et al. 2008b). In particular, Shi et al. (2008b) demonstrate that future Australian rainfall changes are a combined consequence of the long-term trend patterns associated with ENSO, the IOD, and the southern annular mode. Although not clear for other regions, the result for Australia suggests that a realistic simulation of rainfall teleconnections could be important for reducing the uncertainty of climate projections. How well are the teleconnections simulated, and, if there are deficiencies, what controls them? We will investigate these issues.

2. Model and data

We take twentieth-century climate simulation outputs focusing on the period 1950–99, from one experiment for each of the current 24 GCMs that have taken part in the WCRP CMIP3. Details of these models are summarized in Table 1. The outputs of rainfall and temperature are interpolated onto the same grid, detrended and then stratified into four seasons [December, January, February (DJF); March, April, May (MAM); June, July, August (JJA); September, October, November (SON)]. In each model, an index for ENSO, Niño-3.4 (average SST over 5°S–5°N, 170°–120°W) is generated and a correlation between the index and rainfall is calculated.

To benchmark model performance, we use available observational and reanalysis data. The observed rainfall data, subjected to extensive quality control, are from the Australian Bureau of Meteorology Research Centre (BMRC). Other data used include an updated version of the Hadley Centre Global Sea Ice and Sea Surface Temperature (HadISST) dataset (Rayner et al. 2003). To assess the model performance beyond Australia, reanalysis outputs from the National Centers for Environmental Prediction (NCEP) (Kalnay et al. 1996) are utilized. These datasets are of an equal length to the model outputs, allowing for the comparison of correlations between climate driver indices and circulation fields. For rainfall, we have also used the Climate Prediction Center Merged Analysis of Precipitation (CMAP) (Xie and Arkin 1997) to examine the models' performance in simulating rainfall climatology.

TABLE 1. Models names, identifications (IDs), and their origins.

Model	Institute	IPCC ID
BCCR-BCM2.0	Bjerknes Centre for Climate Research	BCCR-BCM2.0
CCCMA CGCM3.1(T47)	Canadian Centre for Climate Modeling and Analysis	CGCM3.1(T47)
CCCMA CGCM3.1(T63)	Canadian Centre for Climate Modeling and Analysis	CGCM3.1(T63)
Centre National de Recherches Météorologiques Coupled Global Climate Model, version 3(CNRM-CM3)	Centre National de Recherches Météorologiques (France)	CNRM-CM3
CSIRO Mk3.0	CSIRO Marine and Atmospheric Research (Australia)	CSIRO Mk3.0
CSIRO MK3.5	CSIRO Marine and Atmospheric Research	CSIRO Mk3.5
GFDL CM2.0	Geophysical Fluid Dynamics Laboratory (United States)	GFDL CM2.0
GFDL CM2.1	Geophysical Fluid Dynamics Laboratory	GFDL CM2.1
GISS-AOM	Goddard Institute for Space Studies (United States)	GISS-AOM
GISS Model E-H	Goddard Institute for Space Studies	GISS-EH
GISS Model E-R	Goddard Institute for Space Studies	GISS-ER
Institute of Atmospheric Physics (IAP) FGOALS-g1.0	Institute of Atmospheric Physics (China)	FGOALS-g1.0
Istituto Nazionale di Geofisica e Vulcanologia (INGV) ECHAM4	Istituto Nazionale di Geofisica e Vulcanologia (Italy)	INGV
INM-CM3	Institute of Numerical Mathematic (Russia)	INM-CM3.0
L'Institut Pierre-Simon Laplace Coupled Model, version 4 (IPSL CM4)	Institute Pierre Simon Laplace (France)	IPSL CM4
MIROC3.2, medium-resolution version (medres)	Center for Climate System Research (Japan)	MIROC3.2(medres)
MIROC3.2(hires)	Center for Climate System Research	MIROC3.2(hires)
Meteorological Institute of the University of Bonn, ECHO-G Model (MIUBECHOG)	Meteorological Institute of the University of Bonn (Germany/Korea)	ECHO-G
Max Planck Institute for Meteorology (MPI) ECHAM5	Max Planck Institute for Meteorology (Germany)	ECHAM5
MRI CGCM2.3.2a	Meteorological Research Institute (Japan)	MRI CGCM2.3.2
National Center for Atmospheric Research (NCAR) CCSM3.0	National Center for Atmospheric Research (United States)	CCSM3
NCAR PCM1	National Center for Atmospheric Research	PCM
UKMO HadCM3	Hadley Centre for Climate Prediction and Research (United Kingdom)	UKMO HadCM3
UKMO HadGEM1	Hadley Centre for Climate Prediction and Research	UKMO HadGEM1

For reference, Fig. 1 plots the annual-mean Indo-Pacific SST and rainfall for the observed (Figs. 1a,b) and averaged over 24 models (Figs. 1c,d) for the period 1950–99 (except for Fig. 1b, where the observed rainfall climatology is calculated over 1979–2006 from CMAP). The model SSTs feature the well-known bias of the equatorial Pacific cold tongue (Davey et al. 2002; Cai et al. 2003), which is too cold and extends too far into the west Pacific. As such, the model maximum SST (i.e., the Pacific warm pool) and the rising branch of the Walker circulation are located too far west. These features persist in all seasons (figures not shown). Most of the observed precipitation falls in the Indian Ocean and over the maritime continents, the equatorial west Pacific, the Northern Hemisphere ITCZ, and the SPCZ (which tilts to the southeast). The model mean rainfall captures these features but produces the double ITCZ, which is another major tropical bias in the coupled GCMs (Lin 2007; Mechoso et al. 1995; Latif et al. 2001; Davey et al. 2002; Meehl et al. 2005). As such, low rainfall occurs along the equator and the model precipitation concentrates over Northern Hemisphere ITCZ and Southern Hemisphere SPCZ. The east–west alignment of the SPCZ is rather unrealistic with the 5 mm day^{-1} contour more zonally orientated than the observed. This is linked to the model SST biases; as can be seen from Fig. 1c, the narrowness of the warm pool and the strong zonal orientation of SST south of the equator are consistent with the rainfall pattern. Previous studies have shown that the double-ITCZ problem is associated with

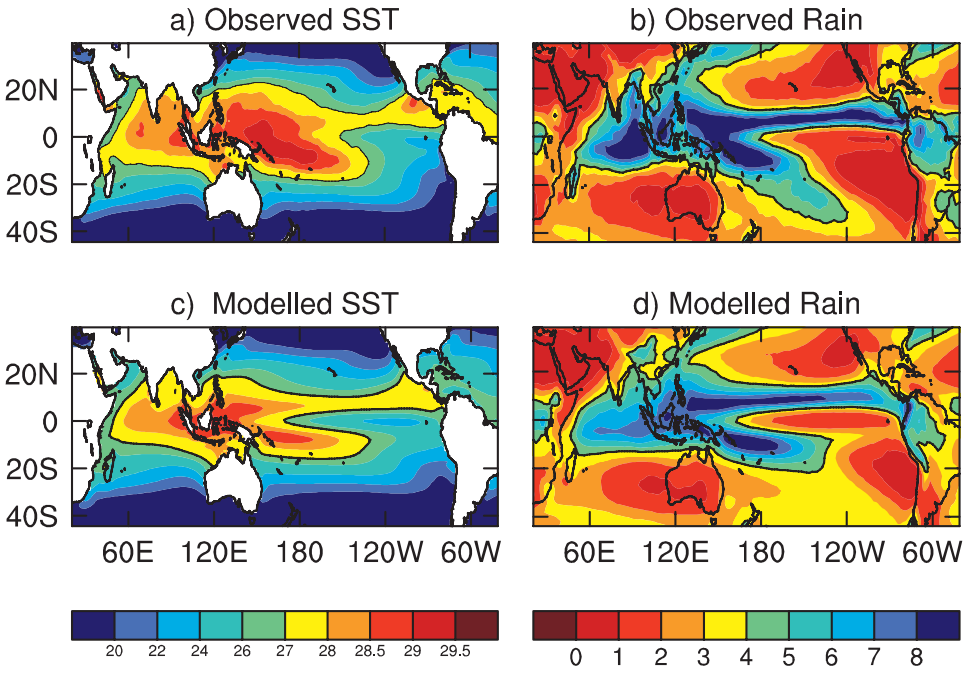

FIG. 1. Climatology of annual-mean (a) SSTs (°C) and (b) rainfall (mm day^{-1}) from the observed compared with the all-model average (c) SST and (d) rainfall. The climatologies for (a),(c), and (d) are calculated across 1950–99, whereas for (b) they are calculated over 1979–2006 (see section 2).

an ocean–atmosphere feedback (Lin 2007). We will show that the unrealistic SST pattern has serious consequences for rainfall teleconnection.

Figure 2 displays the one standard deviation anomaly pattern of ENSO-related SSTs associated with Niño-3.4 for the observed and averaged over all models for MAM and SON. We see that, similar to the climatological mean SST, in these two seasons the anomaly pattern in the models is too narrow in the equatorial Pacific and extends too far west in all seasons. Furthermore, although the model anomalies along the equator are comparable to the observed, they are too weak in the off-equatorial regions. Apart from these biases, the anomaly patterns are reasonably realistic. For example, in DJF (figure not shown) and MAM (Figs. 2a,c), the basin-scale warming anomalies of the Indian Ocean result from El Niño–induced easterly anomalies, which superimpose on the climatological westerlies and reduce the wind speed. Consequently, the weakened latent heat flux and increased surface shortwave radiation act together to warm the Indian Ocean, yielding the basin-scale warm anomaly (e.g., Klein et al. 1999; Alexander et al. 2002; Liu and Alexander 2007). In JJA (figure not shown) and SON (Figs. 2b,d) the patterns in the Indian Ocean are IOD-like although the amplitude is slightly greater than the observed. The relationship between the ENSO–rainfall teleconnection and the IOD–rainfall teleconnection will be discussed in section 5b.

3. ENSO–rainfall teleconnection

We define the ENSO–rainfall teleconnection as the simultaneous correlation between Niño-3.4 and gridpoint rainfall anomalies. Correlation maps are constructed over each season for the observed and for each model. For the Australian region we benchmark model performance using the BMRC's high-quality rainfall data as described in section 2; elsewhere we use NCEP reanalysis.

a. Multimodel ensemble

Averaged over all 24 models, the correlation patterns between Niño-3.4 and gridpoint rainfall (Fig. 3) show several realistic features. First, there is generally higher equatorial and lower off-equatorial rainfall associated with an El Niño, particularly over the cold hemisphere. Second, in JJA and SON, a lower rainfall anomaly over the eastern Indian Ocean associated with El Niño is generated because some of the pIOD events occur coherently with El Niño and vice versa. Nevertheless, there is ample room for improvements. In the first case, the all-model average displays too low a correlation in most locations that is not significant at the 95% confidence level. For example, although many models produce an all-season rainfall reduction over eastern Australia during an El Niño, in the all-model average

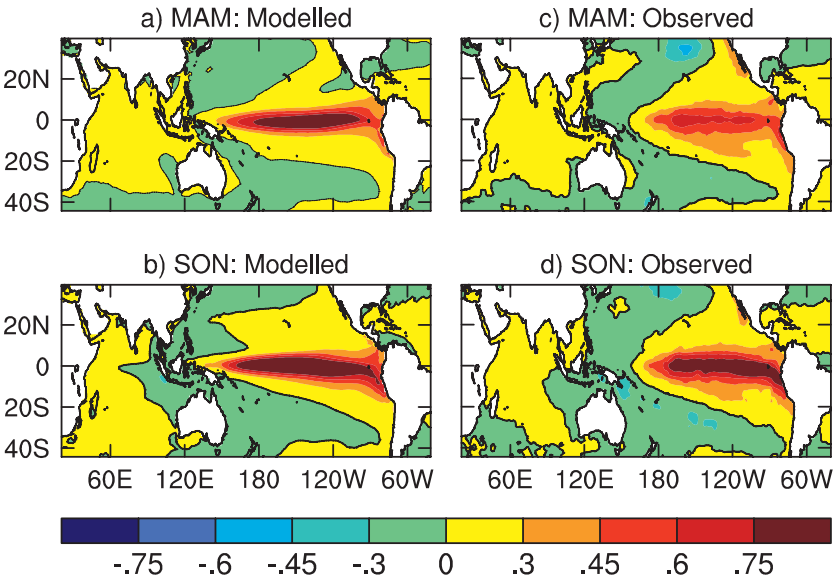

FIG. 2. One standard deviation SST anomaly pattern (°C) associated with Niño-3.4 averaged over 24 models for (a) MAM and (b) SON, compared with the observed in (c) MAM and (d) SON based on HadISST. For each model, detrended gridpoint monthly SST anomalies are first regressed onto a detrended time series of Niño-3.4 to obtain a regression coefficient, which is then multiplied by the one standard deviation of the Niño-3.4 index. Patterns for DJF and JJA are similar to those for MAM and SON, respectively.

this teleconnection is only significant in SON. Similarly, an observed El Niño is associated with a reduction in JJA rainfall over southern India and in DJF rainfall over tropical South America, but teleconnections over the two regions are not statistically significant in the all-model average. Third, minimum correlations that are rather prominent and unrealistic in the central and eastern equatorial Pacific are seen in all seasons. Fourth, the off-equatorial correlations, which are too weak, are situated in latitudes that are too close to the equator. Finally, positive correlations west of the international date line (meaning a rainfall increase during an El Niño) also extend too far west, leading to an overly strong teleconnection, particularly over western Papua New Guinea in DJF (Fig. 3e). In association, poleward of the equatorial west Pacific, negative correlations in DJF and MAM (i.e., a reduction in rainfall associated with an El Niño) also extend too far west into the Indian Ocean, resulting in correlations over the northeastern Indian Ocean that are opposite to the observed. As will be discussed in section 5, many of these features are directly attributable to deficiencies in the Pacific climatological SST simulations seen in Fig. 1 and an ENSO anomaly pattern too equatorially confined and extending too far west.

For JJA and SON, the impact of these deficiencies appears not to be as severe, and the teleconnection patterns over the west Pacific and the eastern Indian Ocean are quite realistic. In these two seasons, ENSO and the IOD may occur concurrently. We will discuss the simulation of the IOD–rainfall teleconnection and its relationship with the ENSO–rainfall teleconnection in section 4.

b. *Intermodel differences*

For a given season, there are strong differences on a model-to-model basis, and often readers require information about the performance of individual models in their regions of interest. Figure 4 displays maps of the austral summer ENSO–rainfall teleconnection for each of the 24 GCMs. In the equatorial Pacific region, where positive correlations are too weak in many models, some models actually generate negative correlations, opposite to the observed [Bjerknes Centre for Climate Research Bergen Climate Model version 2.0 (BCCR-BCM2.0) Fig. 4g; Met Office Hadley Centre Global Environmental Model version 1 (UKMO HadGEM1) Fig. 4h]. Near eastern Australia the teleconnection differs from models with very weak or nonexistent correlations [e.g., Fig. 4f Goddard Institute for Space Studies Model E-H (GISS-EH)] to ones that are too strong [e.g., Fig. 4x Flexible Global Ocean–Atmosphere–Land System Model gridpoint version 1.0 (FGOALS-g1.0)]. More models simulate an ENSO–rainfall teleconnection stronger over northwest Australia (NWA) than over eastern Australia.

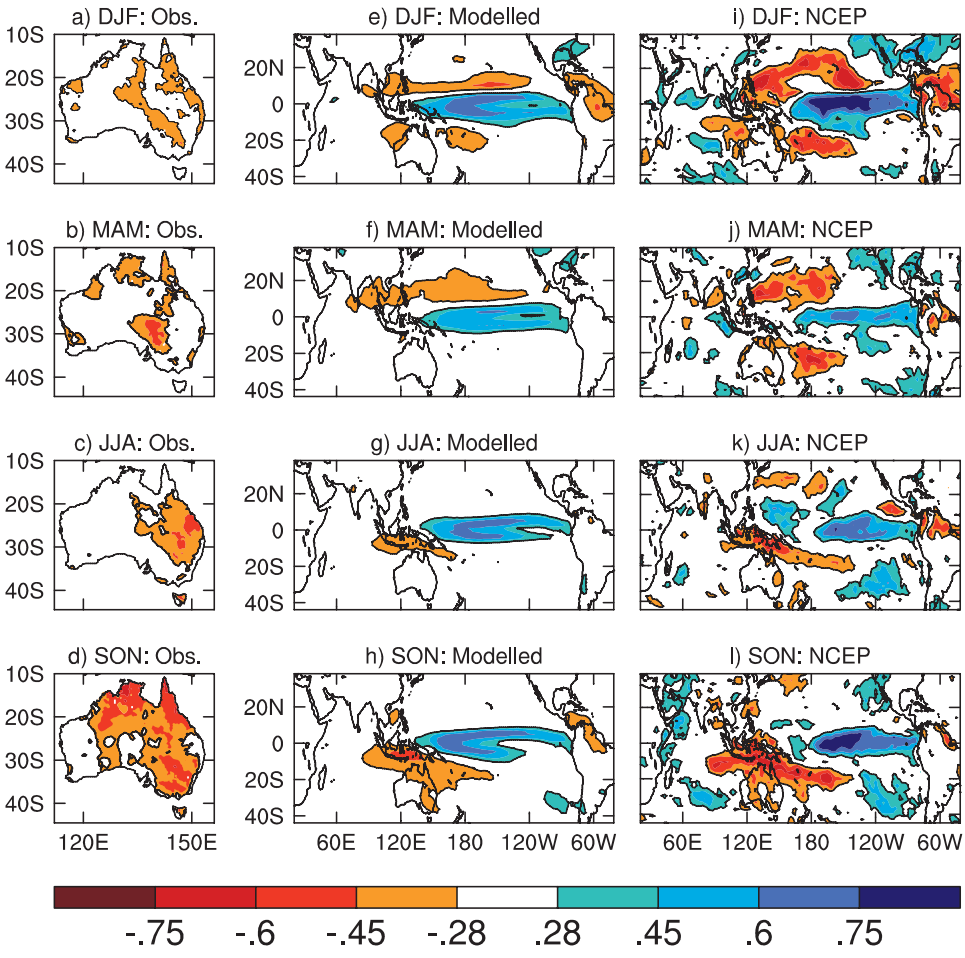

FIG. 3. Correlation between HadISST Niño-3.4 and gridpoint Australian rainfall for (a) DJF, (b) MAM, (c) JJA, and (d) SON. (e)–(h) The same as (a)–(d) but averaged over 24 models. (i)–(l) The same as (a)–(d) but based on NCEP rainfall (with HadISST Niño-3.4). A correlation with an absolute value greater than 0.28 is statistically significant at the 95% confidence level.

This appears to be linked to the models' west Pacific warm pool and the rising branch of the Walker circulation extending too far west (Fig. 1). As the warm pool position oscillates westward and eastward (with ENSO cycles) from its mean position, the ENSO–NWA rainfall relationship tends to be too strong, as in the Commonwealth Scientific and Industrial Research Organisation Mark version 3.0 (CSIRO Mk3.0) model (Shi et al. 2008b). In reality, ENSO mainly influences eastern and northeast Australian climate variability.

Similarly, strong intermodel differences are produced in SON (Fig. 5). For example, although the teleconnection over southeast Australia (SEA) is overly strong in a number of models [CSIRO Mk3.5 (Fig. 5r), Geophysical Fluid Dynamics Laboratory Climate Model version 2.0 (GFDL CM2.0) (Fig. 5u), and FGOALS-g1.0 (Fig. 5x)], there are more models generating a weaker teleconnection than the observed [e.g., BCCR-BCM2 (Fig. 5f); Canadian Centre for Climate Modelling and Analysis (CCCma) Coupled General Circulation Model, version 3.1 (CGCM3.1 T47) (Fig. 5d); UKMO HadGEM1 (Fig. 5l); and Meteorological Research Institute Coupled General Circulation Model, version 2.3.2 (MRI CGCM2.3.2) (Fig. 5n)]. As a result, the all-model average teleconnection is too weak over SEA.

Figures 4 and 5 are organized in the order of ENSO amplitude measured by the one standard deviation value of Niño-3.4, increasing down each column and from the left to right. The results indicate that the ENSO amplitude is an important controlling factor: as the ENSO amplitude increases from model to model the ENSO–rainfall teleconnection generally strengthens. To further illustrate this point, we plot intermodel variations of the ENSO amplitude against intermodel variations of ENSO–rainfall teleconnection for several regions within and outside continental Australia (Figs. 6 and 7, respectively;

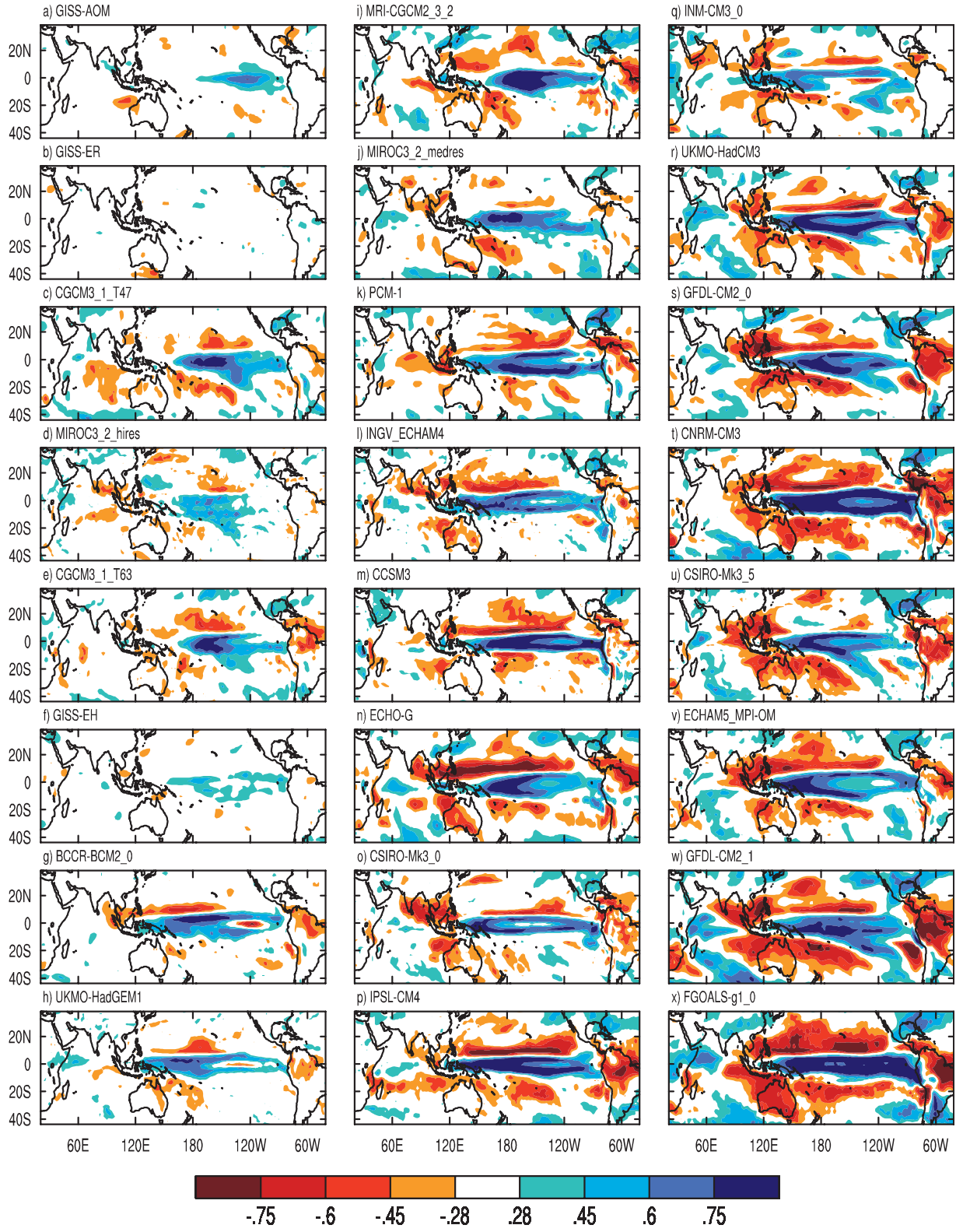

FIG. 4. Correlation between gridpoint rainfall and Niño-3.4 for DJF for each model. A correlation with an absolute value greater than 0.28 is statistically significant at the 95% confidence level. The panels are arranged showing models with increasing Niño-3.4 standard deviation from top to bottom in each column and from left to right.

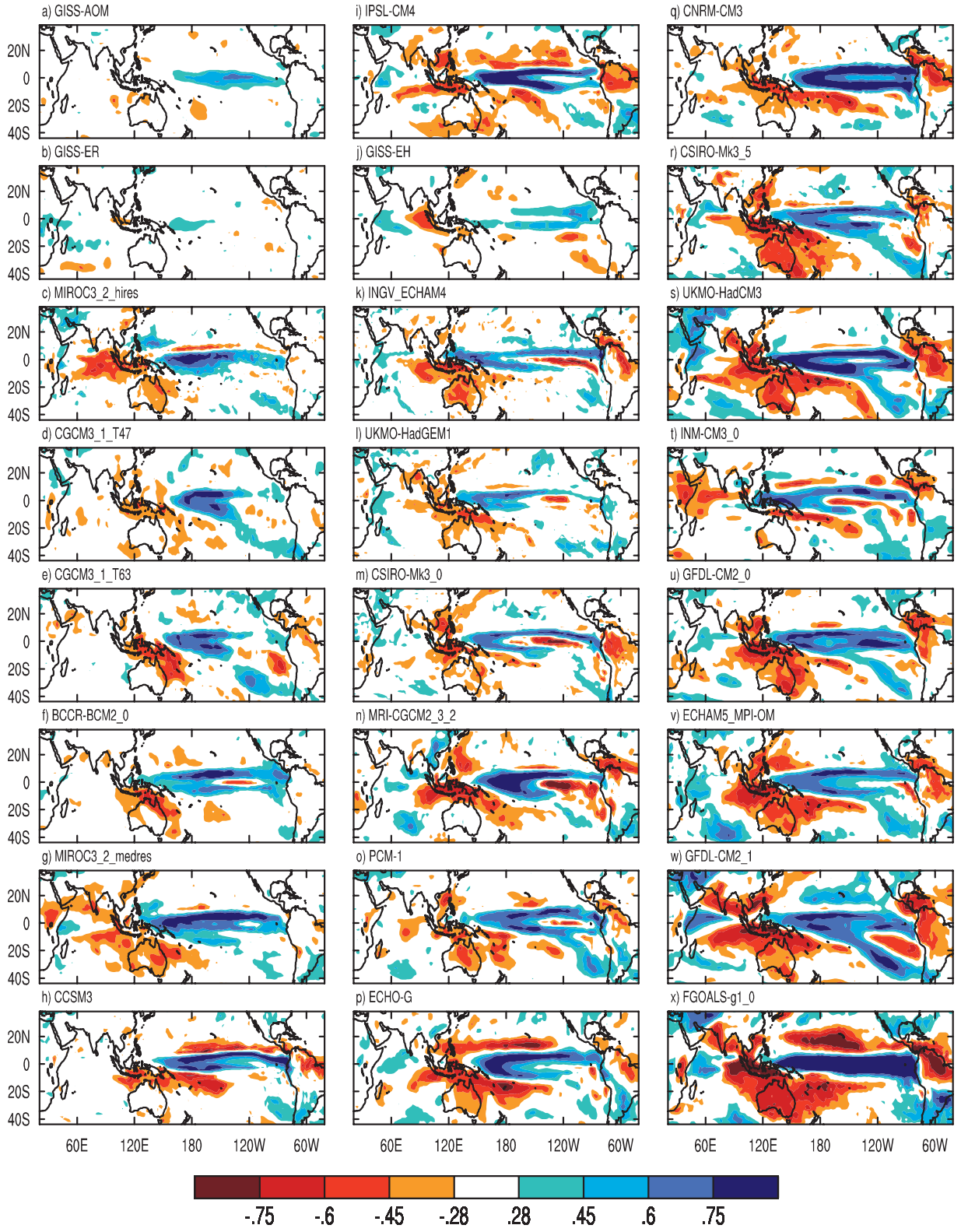

FIG. 5. The same as Fig. 4 but for SON.

see figure caption for region details). They reflect several features embedded in Fig. 3, including a large number of models that have quite a weak ENSO–rainfall teleconnection over southeast Queensland (SEQ) in DJF (Fig. 6a), over SEA in SON (Fig. 6c), over southern India in JJA (Fig. 7a), and over the Sumatra–Java region in SON (Fig. 7c) but too strong a teleconnection over NWA in DJF (Fig. 6b).

In each of these plots, the correlation between intermodel variations of the ENSO–rainfall teleconnection and intermodel variations of the ENSO amplitude is shown. Assuming that each model is an independent sample, a correlation coefficient (labeled ''correl'' in each panel of Figs. 6 and 7) with an absolute value greater than 0.4 indicates statistical significance at the 95% confidence level. In all cases selected here, such a significance level is achieved. Thus the control on the ENSO–rainfall teleconnection by the ENSO amplitude is systematic, highlighting the importance of realistically simulating this attribute.

In an atmospheric intermodel comparison framework, Scaife et al. (2008) show that the sensitivity of the Southern Oscillation index (SOI) to Niño-3 SST changes vastly from one model to another (their Fig. 4, lower panel). Regressing rainfall in affected regions onto Niño-3.4 (figure not shown) indicates that this is also the case. This is not contradictory to our result of a control by ENSO amplitude on the ENSO–rainfall correlation, which only measures coherence.

In models with a stronger ENSO amplitude, the rainfall variability is more likely to be overwhelmed by ENSO-induced signals. To illustrate this, we define ''signal'' as the standard deviation associated with Niño-3.4 [given as $S_{\mathrm{ENSO}}(x, y, k)$; k representing each of the 24 models, determined from a linear regression onto the Niño-3.4 index] and ''noise'' as the standard deviation of the residual after removing ENSO-induced rainfall signals [given as $N_{\mathrm{ENSO}}(x, y, k)$]. This is calculated for each season to generate the ratio $R_{\mathrm{ENSO}}(x, y, k) = S_{\mathrm{ENSO}}(x, y, k)/N_{\mathrm{ENSO}}(x, y, k)$. A simple manipulation shows that, for a given location, the ratio has a mathematical expression of $R_{\mathrm{ENSO}} = S_{RE}/\sqrt{S_{RR}S_{EE} - S_{RE}}$ compared with that for the teleconnection with ENSO of $\mathrm{TC}_{\mathrm{ENSO}} = S_{RE}/\sqrt{S_{RR}S_{EE}}$, where S_{RE}, S_{RR}, and S_{EE} are the rainfall–ENSO covariance and the variance of rainfall and ENSO, respectively. The difference in the two expressions indicates that the ratio is far more sensitive to the covariance than the correlation and therefore increases nonlinearly with the coherence.

Figure 8 plots the intermodel variations of ENSO amplitude against intermodel variations of the ratio for some of the regions discussed in Figs. 6 and 7. The greater the ENSO amplitude, the greater the ratio of ''signals to noise.'' It follows that the ratio provides a stronger control over the ENSO–rainfall teleconnection than the ENSO amplitude, as illustrated in Fig. 9. This is because it is a description not only of the ENSO-induced rainfall signals but also its relative strength to stochastic noise. The relationship between the intermodel variations of the ratio and the intermodel variations of the ENSO–rainfall teleconnection is strong and has a correlation greater than 0.9, statistically significant at the 99% confidence level.

Before we leave this section, a brief summary is in order. There are significant intermodel differences in terms of the strength and spatial pattern of the ENSO–rainfall teleconnection. The dominant influence is the amplitude of rainfall variations due to ENSO relative to stochastic noise, which seems to control the strength of the teleconnection. In section 5, we will further discuss factors controlling the spatial pattern.

4. IOD–rainfall teleconnection

a. Model IOD and its index

The simulation of the IOD in the CMIP3 models has been comprehensively examined by Saji et al. (2006) in terms of an influence from a mean state, spatial pattern, seasonality, and forcing. In their study, the index of the IOD was represented by the leading component of the anomalous 20°C isotherm depth in an Indian Ocean domain of 20°S–20°N. This is a modified form of the Shinoda et al. (2004) IOD index, which uses the leading component of ocean temperature anomalies in the equatorial depth plane. The advantage of these indices over a separate index defined as the large-scale zonal SST gradient between the western and eastern Indian Ocean (Saji et al. 1999) is that it does not impose the dipolar structure in the SST anomalies, which allows each model to show an IOD-like pattern of its own. Ideally we would use an SST-based index for investigating the IOD–rainfall teleconnection, as SSTs are an effective medium whereby impacts of the ocean are communicated to the atmosphere. As such, in the present study, our IOD index is defined as the leading component of SST anomalies in the Indian Ocean between 20°S and 20°N. Empirical orthogonal function (EOF) analysis was carried out for each season and for each model. In our EOF analysis, the variance is expressed in the EOF pattern, the principal component being scaled to unity, that is, with a standard deviation of one.

The majority of models feature an IOD pattern that starts to develop in JJA with cooler SSTs in the east, and peaks in SON, as in the observed. Saji et al. (2006) show that this results from a GCMs' ability to simulate the

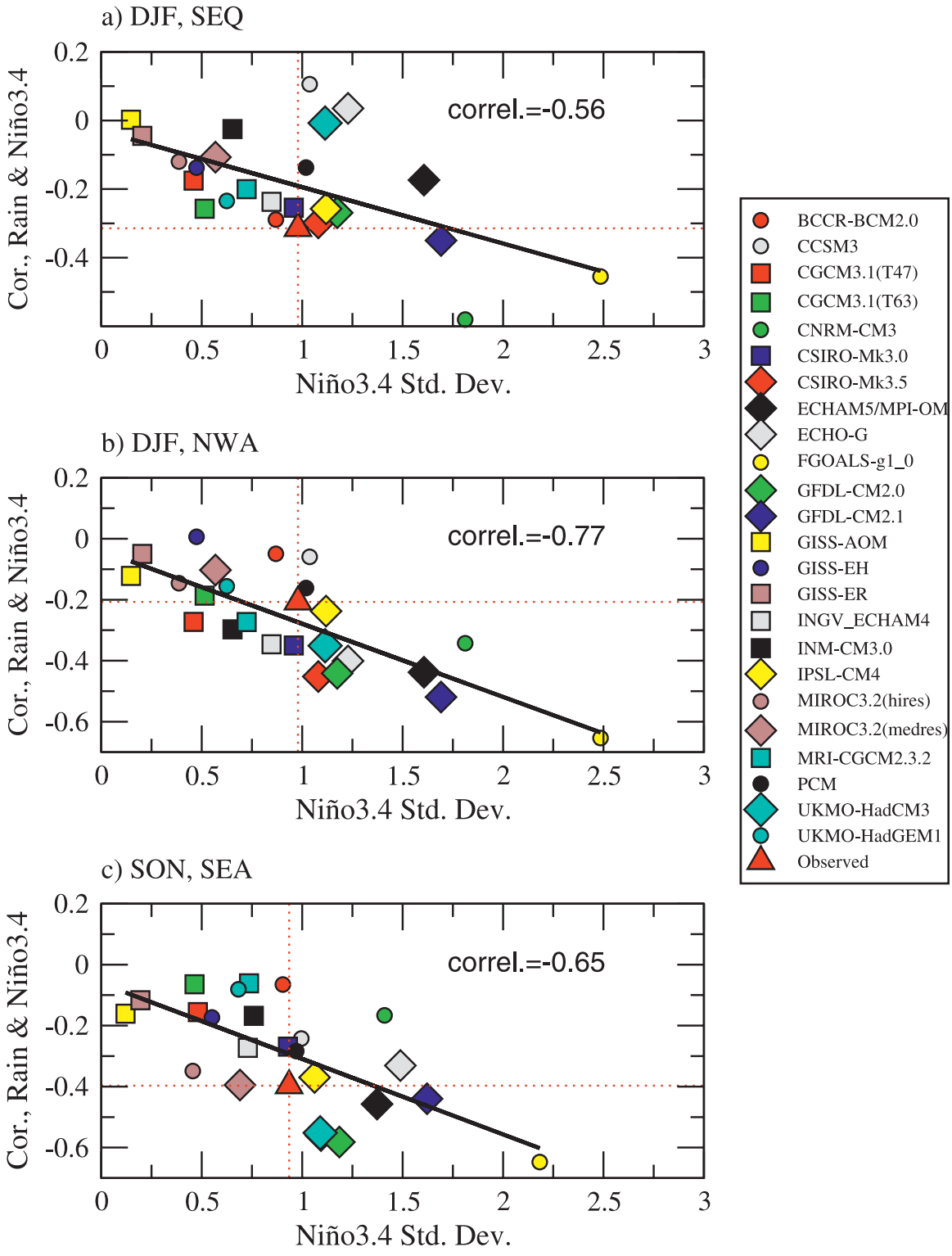

FIG. 6. Scatterplot of intermodel variations of Niño-3.4 correlations with rainfall against intermodel variations of the amplitude of ENSO (as measured by the one standard deviation value of Niño-3.4) for (a) DJF in the SEQ region (20°–30°S, 150°–155°E), (b) DJF in the NWA region (10°–30°S, 110°–135°E), and (c) SON in the SEA region (30°–38°S, 140°–155°E). The slope and correlation of a linear fit are presented. Assuming each model is independent, a correlation with an absolute value greater than 0.40 is statistically significant at the 95% confidence level.

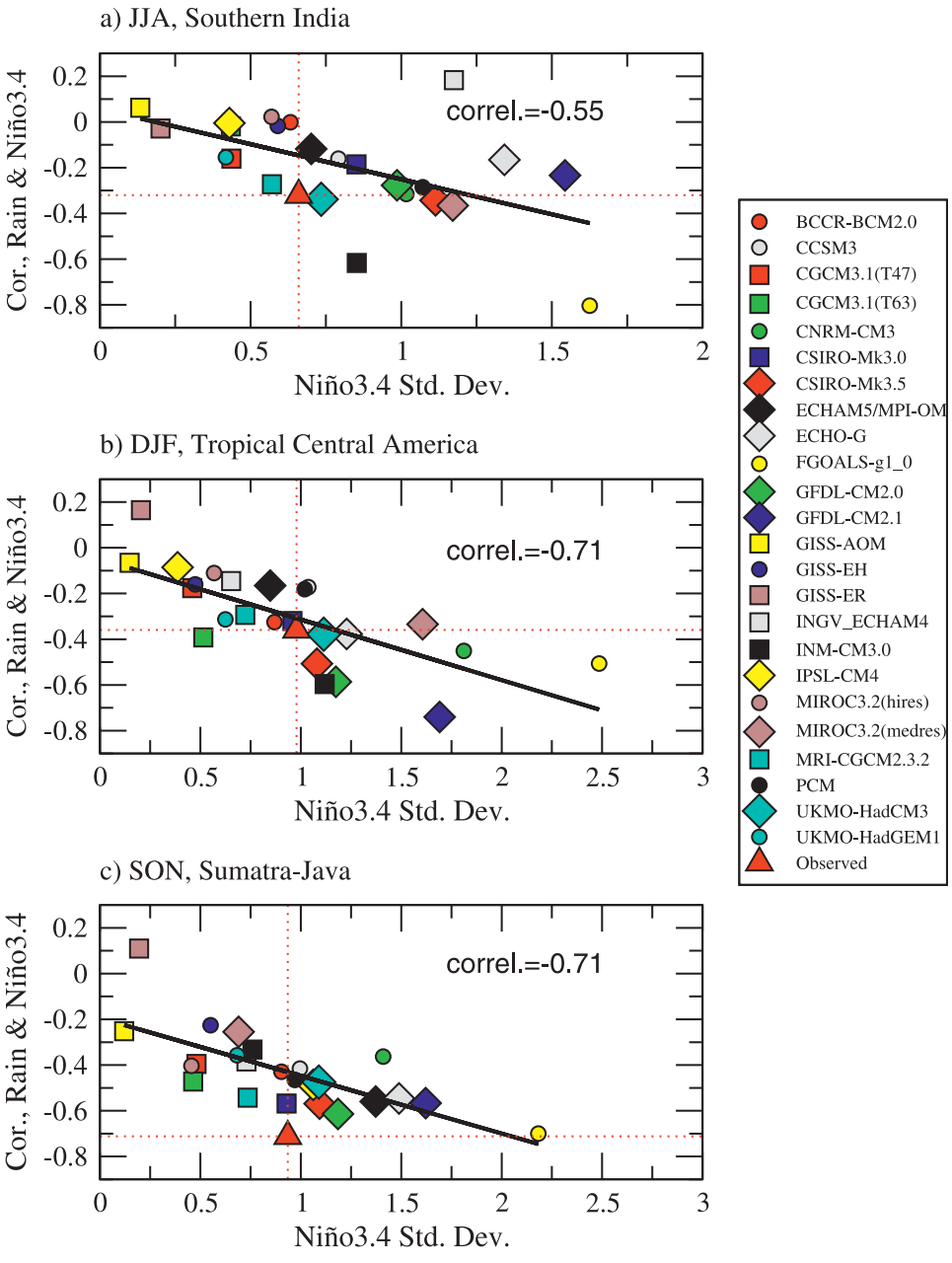

FIG. 7. The same as Fig. 6, but for (a) JJA rainfall in southern India (9°–15°N, 74°–84°E), (b) DJF rainfall in tropical Central America (5°–5°N, 280°–320°E), and (c) SON rainfall over the Sumatra–Java region (10°S, 124°E).

seasonal cycle of the Indian Ocean, in which observed upwelling-favorable winds are generated off the Sumatra–Java coast in June–October, essential for an IOD to develop (Xie et al. 2002). The model IOD pattern in SON is shown in Fig. 10. It is not a trivial task for a coupled model to simulate the IOD because the monsoons, ENSO, and the internal air–sea processes all have an important role in generating SST variability. Given that it is the zonal SST gradient that is important in terms of shifting atmospheric convection, it is not unusual to see the majority of models produce an IOD-like anomaly in terms of the gradient. An exception is GISS Model E-R (GISS-ER) (Fig. 10b), which features a generally uniform warming pattern throughout the entire Indian Ocean basin. These models can be classified into four groups. One group features a dominance by negative anomalies in the eastern Indian Ocean, such as the Community Climate System Model, version 3 (CCSM3)

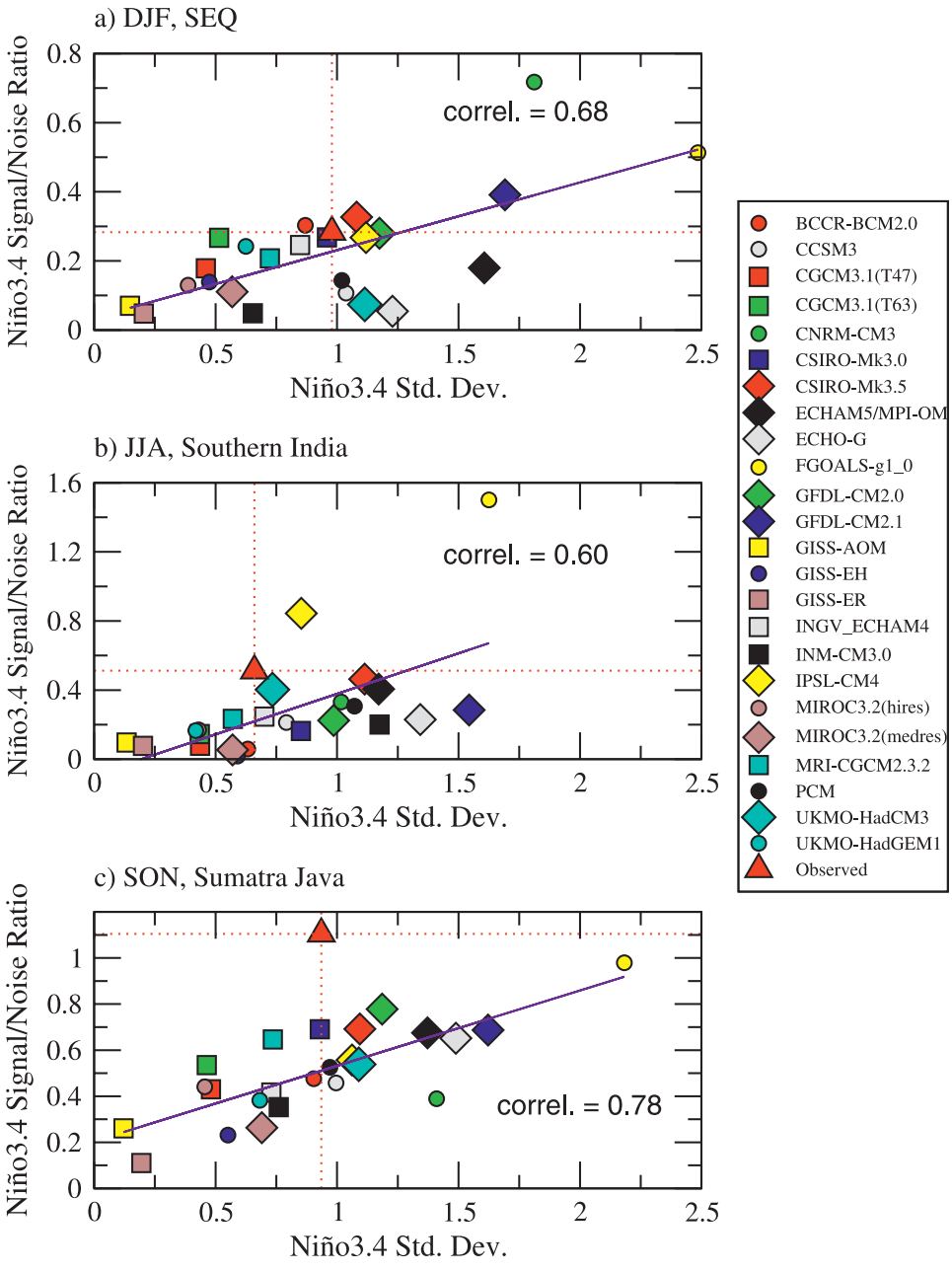

FIG. 8. The same as Fig. 6, but for ENSO amplitude against "signal-to-noise ratio," for (a) SEQ in DJF, (b) southern India in JJA, and (c) the Sumatra–Java region in SON. See text for the definition of "signal-to-noise ratio."

(Fig. 10c); CGCM3.1 T63 (Fig. 10e); and Model for Interdisciplinary Research on Climate 3.2, high-resolution version [MIROC3.2(hires)] (Fig. 10o). The second group is characterized by weak but scattered anomalies in the eastern Indian Ocean, for example, ECHAM and the global Hamburg Ocean Primitive Equation (ECHO-G) (Fig. 10d) and Institute of Numerical Mathematics Coupled Model, version 3.0 (INM-CM3.0) (Fig. 10p). The third group shows an overall lack of variability, and this group includes GISS Atmosphere–Ocean Model (GISS-AOM) (Fig. 9a) and GISS-ER (Fig. 9b). The final group simulates an eastern cold tongue anomaly that is too strong [e.g., Parallel Climate Model (PCM) (Fig. 10t) and GFDL CM2.1 (Fig. 10x)]. Averaged over all models, the anomaly in the eastern pole is too strong (Fig. 10z) but resembles the observed pattern (Fig. 10y).

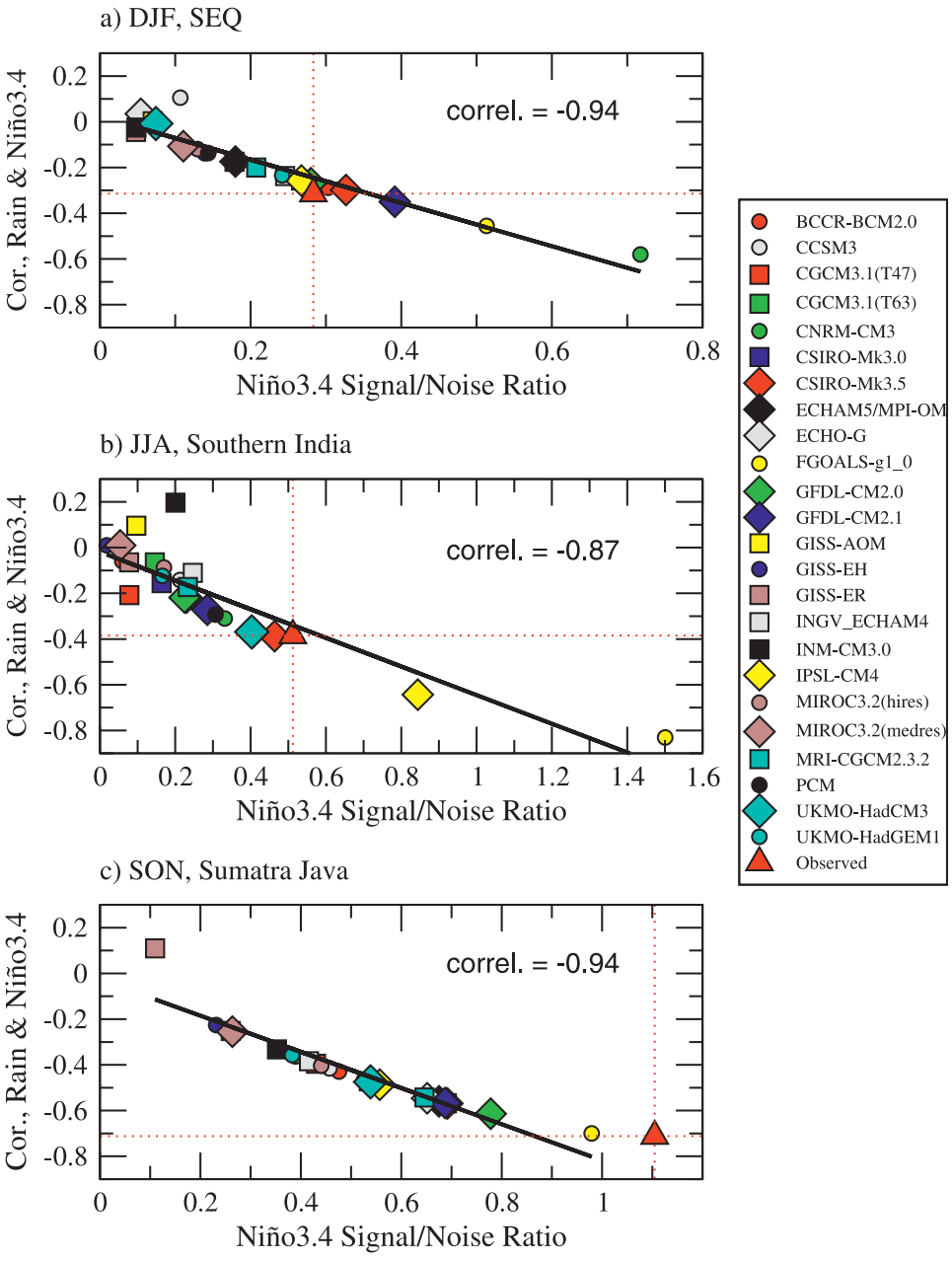

FIG. 9. The same as Fig. 6, but for "signal-to-noise ratio" against ENSO–rainfall correlation, for (a) SEQ in DJF, (b) southern India in JJA, and (c) the Sumatra–Java region in SON.

The leading patterns in DJF and MAM (not shown) are basically the basin-scale modes associated with ENSO (e.g., Klein et al. 1999; Yulaeva and Wallace 1994; Alexander et al. 2002). One exception is the PCM model, in which the leading EOF is also IOD-like, similar to its EOF1 pattern in SON. It shows resemblance to an early version of the CSIRO model (not included in the present study) as reported in Shi et al. (2008a). In that CSIRO model, the IOD-like variability pattern is a consequence of the model cold tongue extending into the Sumatra–Java coast, resulting in the coastal region forming a part of the west Pacific warm pool.

b. IOD–rainfall teleconnection

Maps of the IOD–rainfall teleconnection for JJA and SON are constructed through correlation analysis between the IOD index with gridpoint rainfall anomalies. Figure 11 shows maps from the observed (Figs. 11a,b)

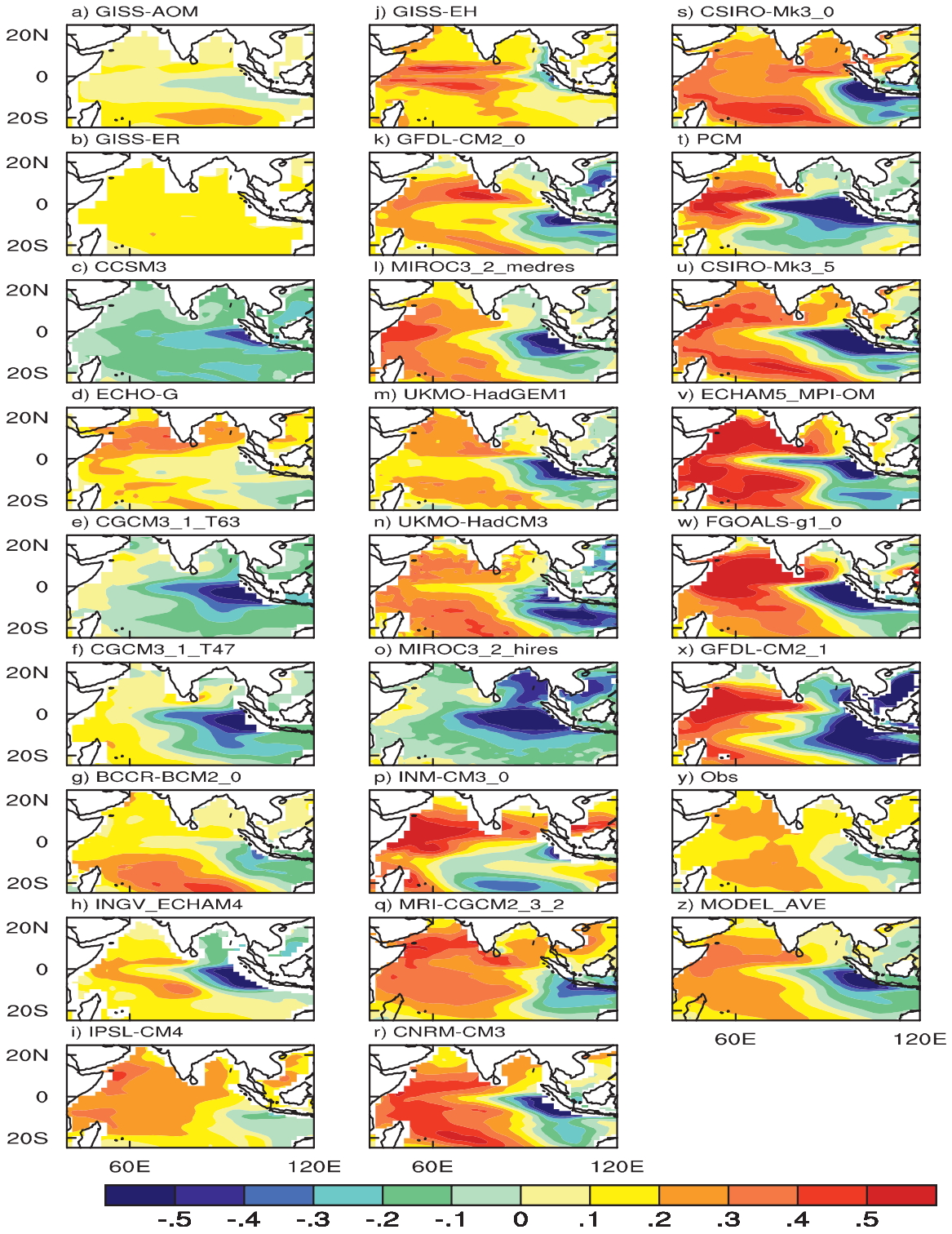

FIG. 10. EOF1 patterns of SST anomalies for SON in the Indian Ocean domain of 20°S–20°N for the 24 models (a)–(x). Also shown are the EOF1 patterns from the observed (y) and the average model pattern (z). The intermodel variations of the variances are reflected in the patterns shown above, with the standard deviation of associated time series equal to one. These patterns are arranged in terms of the order of EOF variances, increasing top to bottom in each column and from left to right.

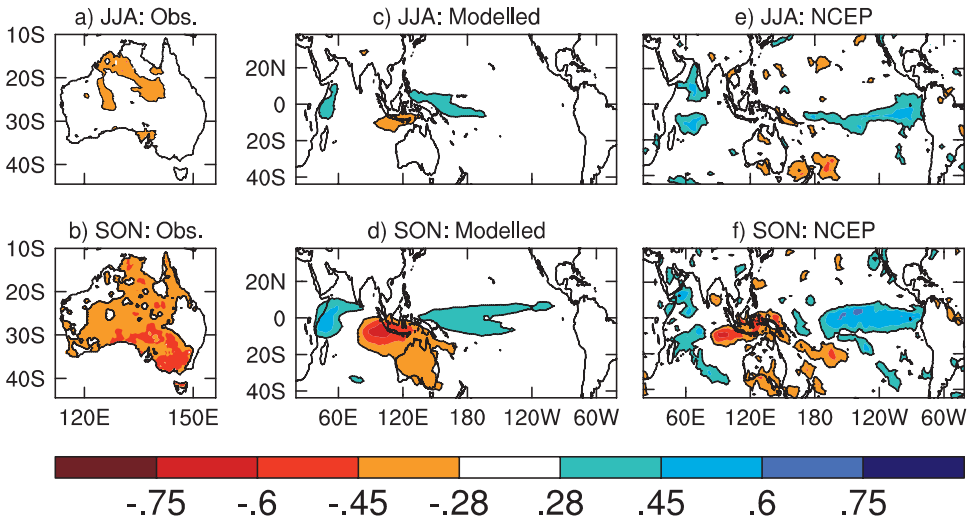

FIG. 11. Correlation between an IOD index (time series of the Indian Ocean SST EOF1 taken from HadISST) and gridpoint Australian rainfall in (a) JJA and (b) SON. (c),(d) The same as (a) and (b) but for a 24-model ensemble average. (e),(f) The same as (a) and (b) but based on NCEP rainfall (with HadISST). Only absolute values greater than 0.28 are plotted, which are statistically significant at the 95% confidence level.

averaged over all models (Figs. 11c,d) and based on NCEP (Figs. 11e,f). In JJA, the teleconnection is generally weak; this is the case over much of SEA (Figs. 11, top panels). In SON (Figs. 11, lower panels), a pIOD is associated with a decrease in rainfall over SEA, the Sumatra–Java region, and East Africa. These IOD impacts have been explored in previous studies (Ashok et al. 2001; Black et al. 2003; Zubair et al. 2003; Yamagata et al. 2004; Cai et al. 2005). Compared with the teleconnection pattern from the NCEP reanalysis, the modeled teleconnection over the eastern Indian Ocean is realistic in size (Figs. 11d,f) but too weak over SEA (Figs. 11b,d). As will be discussed below, the latter feature is in part due to the lower level of coherence between the IOD and ENSO in the models compared with the observed. Furthermore, the maximum correlations occur over the equatorial west Pacific instead of the central and equatorial Pacific region (Figs. 11b,d)—a feature that is associated with ENSO SST anomalies extending too far west.

c. *Intermodel differences*

Similar to the ENSO–rainfall teleconnection, there are strong intermodel differences with respect to the IOD–rainfall teleconnection. Figure 12 plots the SON maps, following the order of increasing IOD amplitude (square root of the sum of the variance in spatial weights in EOF1 shown in Fig. 10) down each column and from left to right. The feasibility of using the SST EOF1 time series is confirmed by the fact that all models produce a negative correlation with rainfall in the eastern Indian Ocean, meaning that, as SSTs in the eastern Indian Ocean cool, rainfall in that region reduces.

Compared with Fig. 5, the order of models changes significantly. Such a change underscores an overall weak coherence between ENSO and the IOD. If the IOD is a mere slave of ENSO then one would expect the order of the models to be the same. Although for a given location the strength of the teleconnection differs vastly, and a clear relationship of a stronger IOD associated with a stronger IOD–rainfall teleconnection emerges (Fig. 13). Similar to the process associated with ENSO, the stronger the IOD amplitude and the IOD signal relative to the noise, the better the IOD influence on rainfall is manifested, as shown in Fig. 14 for SEA, Sumatra–Java, and East Africa. The control on intermodel variations of the IOD–rainfall teleconnections by intermodel variations of the IOD rainfall signal-to-noise ratio is rather strong, with a correlation close to or above 0.9 (not shown).

5. Discussion

In the previous sections, we describe the intermodel variations of the ENSO–rainfall and IOD–rainfall teleconnections in all 24 models. We show that, out of the seemingly disorganized and vast intermodel differences, a systematic relationship exists between intermodel variations of amplitude and its signal-to-noise ratio and intermodel variations of the rainfall teleconnections, underscoring the importance of realistically reproducing these parameters. Below, we highlight factors that influence the rainfall teleconnections patterns.

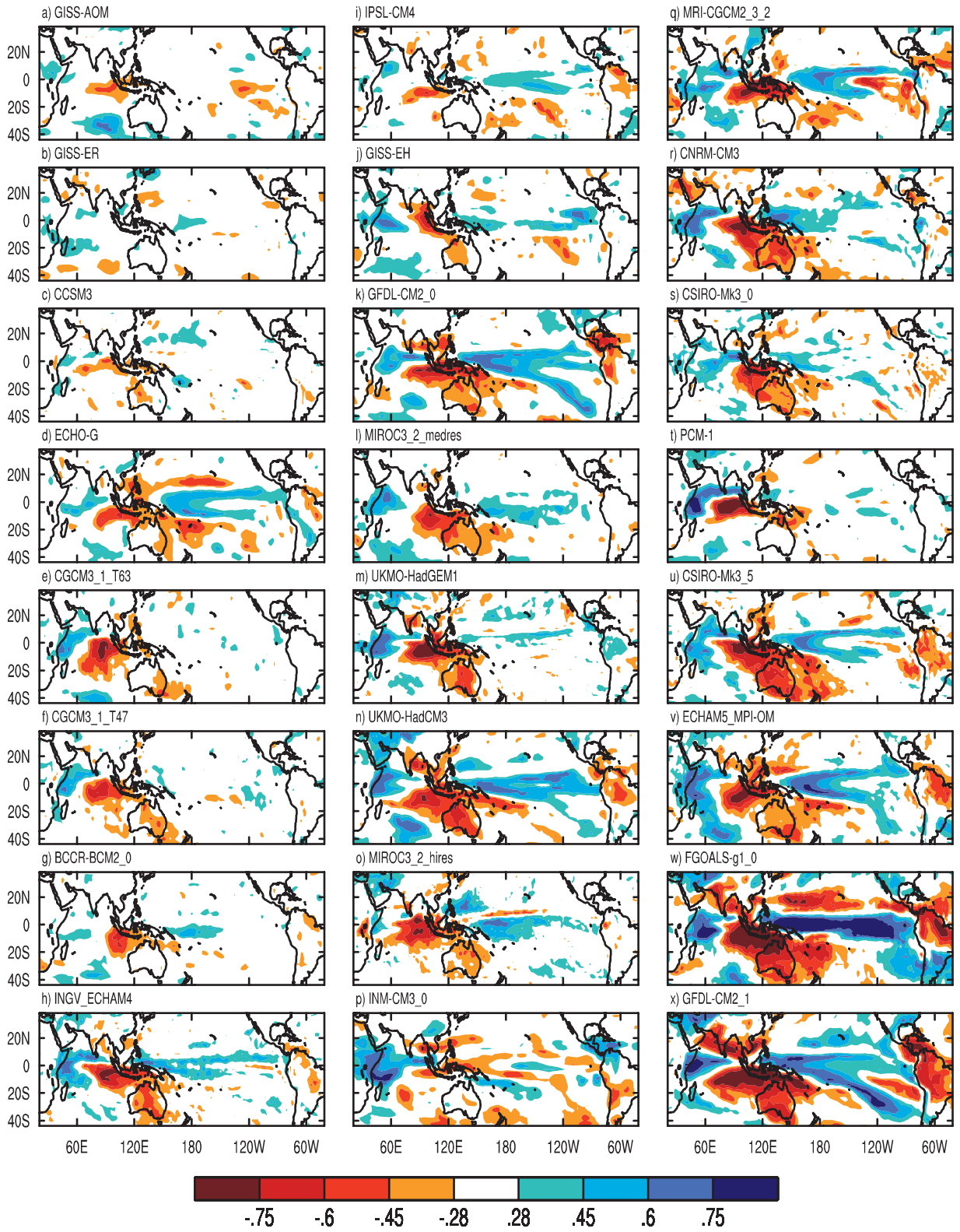

FIG. 12. Correlation between gridpoint rainfall and an IOD index for SON for each model. The panels are arranged (a)–(x) showing models with increasing IOD amplitude, defined as the square root of the total variance of spatial weights in the EOF1.

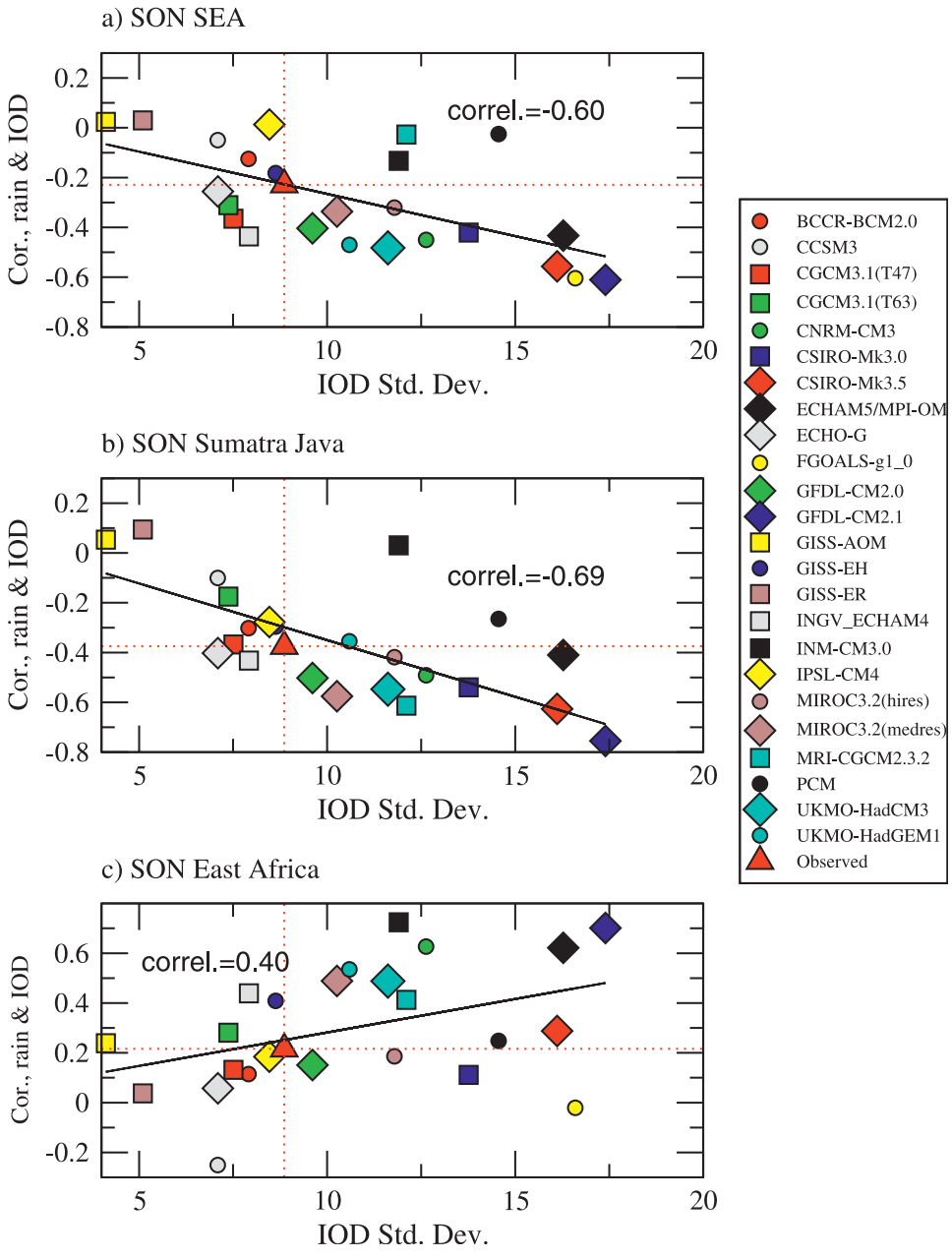

FIG. 13. Scatterplot of intermodel variations of IOD–rainfall correlations against intermodel variations of IOD amplitude for (a) SEA, (b) the Sumatra–Java region, and (c) eastern Africa (5°S–3°N, 38°–40°E).

a. Impact of Pacific cold tongue bias on ENSO–rainfall teleconnection

As discussed in the earlier sections, to a large extent differences between the modeled and the observed ENSO–rainfall teleconnection may be attributable to the simulation of the Pacific SST structure and the consequential ENSO anomaly pattern. The deficiencies may be discussed in terms of the following aspects: the climatological Pacific SST that is too cold, too narrow, and located too far west—each has significant consequences.

Because the climatological SST over the equatorial central Pacific is too cold, this leads to a reduction in convection. This is already shown in a strip of low climatological rainfall along the equatorial Pacific (Fig. 1), surrounded by the double ITCZ on each side of the equator, as a result of convection moving away from the equator. In association, there are regions in the central and eastern Pacific that show a negligible rainfall

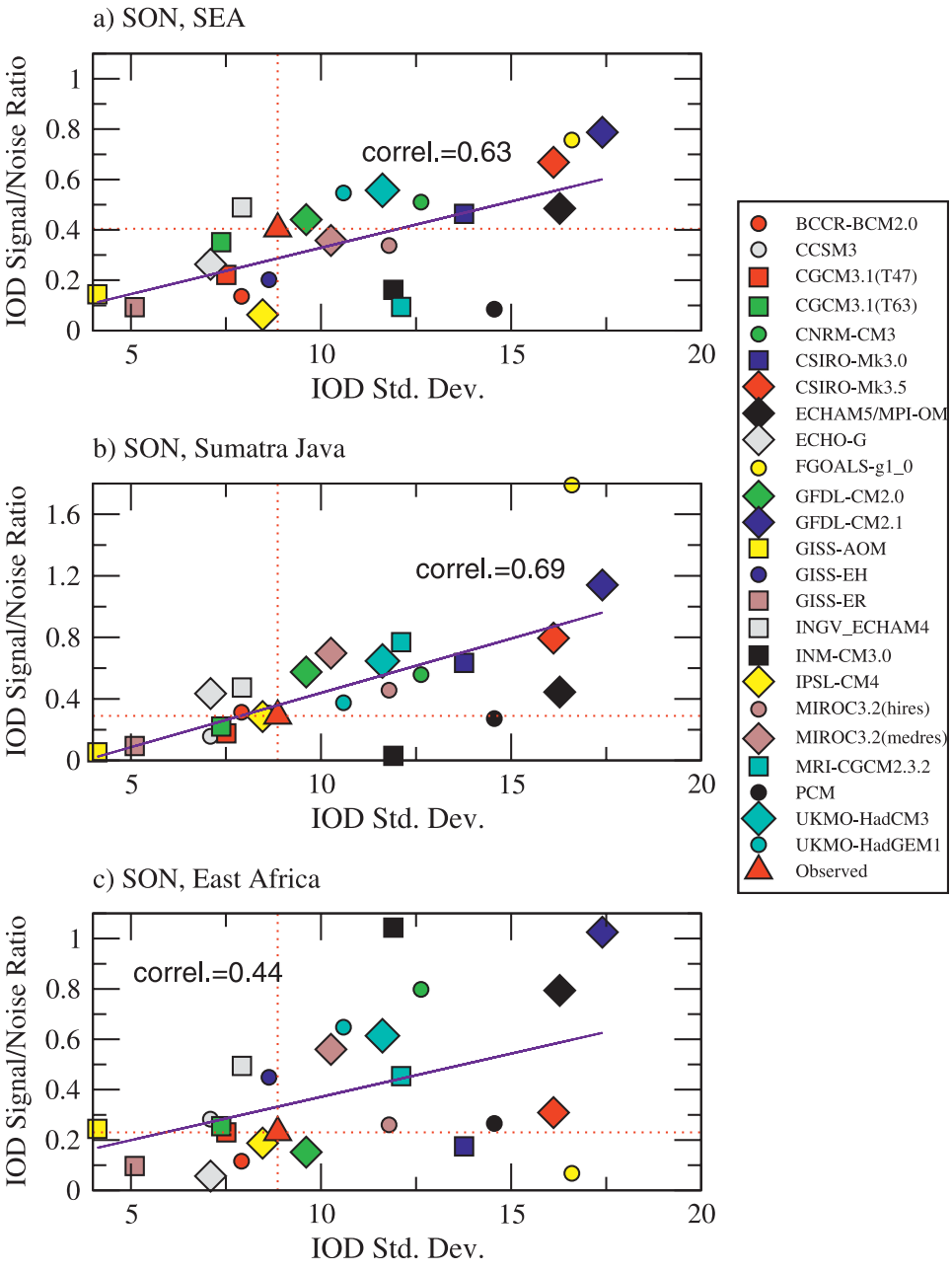

FIG. 14. The same as Fig. 13, but for intermodel variations of IOD rainfall "signal-to-noise ratio" against intermodel variations of IOD amplitude.

response to ENSO (Figs. 3e–h) in many models, and even with an El Niño–induced positive SST anomaly superimposed, the resultant SST along the central and eastern equator is still too cold to shift convection back to the equator. This error is so systematic that in many models the ENSO–rainfall teleconnection does not even respond to the intermodel variations of the ENSO rainfall signal-to-noise ratio (Fig. 9) in this region of the equatorial Pacific.

The narrowness of the Pacific cold tongue anomaly appears to influence the teleconnection beyond ±10° of the equator, where the teleconnection is of an opposing sign to that within the equatorial Pacific. For example, boreal winter rainfall over Hawaii tends to decrease during an El Niño (Fig. 15a), as the ITCZ migrates southward to be anomalously closer to the equator. As a result of the narrow climatological cold tongue, the meridional extent of the ITCZ movement is smaller

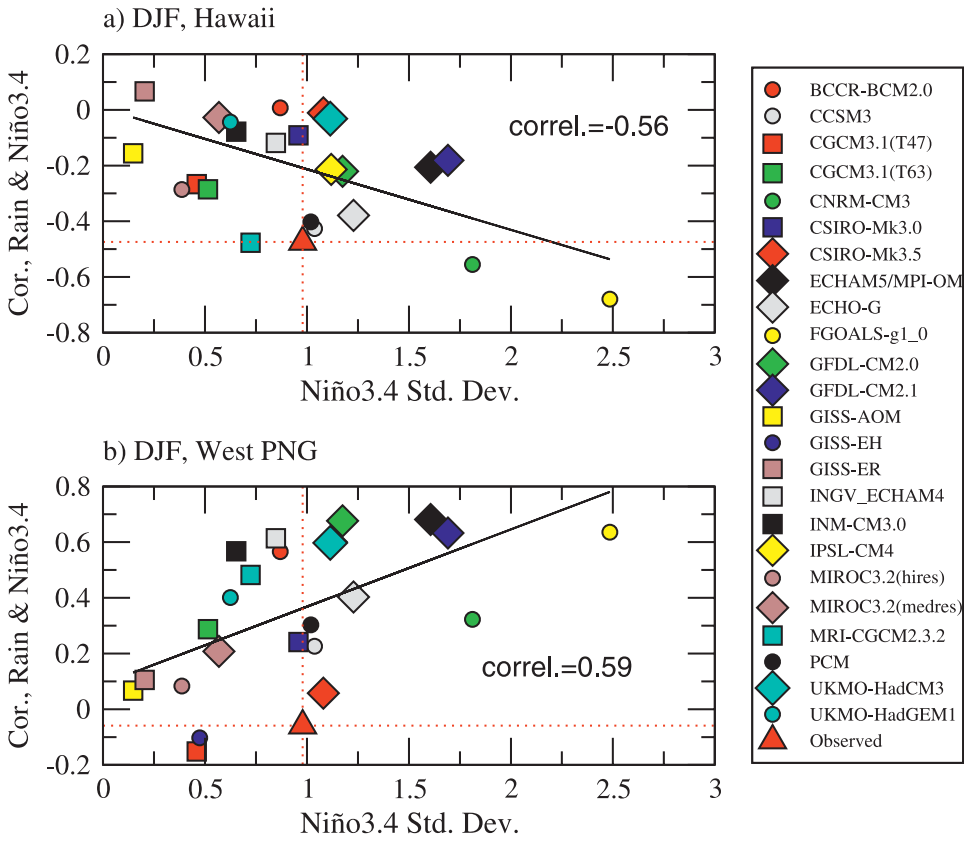

FIG. 15. (a) Scatterplot of DJF intermodel variations of the ENSO–rainfall teleconnection against intermodel variations of DJF Niño-3.4 standard deviation over (a) Hawaii (19.5°N, 204.5°E) and (b) west Papua New Guinea (3°S, 135°E).

(Fig. 3e). The anomalous movement of the ITCZ during ENSO cycles is limited by the smaller meridional extent, which confines the teleconnection pattern toward the equatorial Pacific region. This contributes to an ENSO–rainfall teleconnection outside the Pacific showing up as weaker than the observed.

There are also significant consequences of a climatological cold tongue that is too far west. This also means that the warmest SST is located too far west. As a result, the model maximum rainfall over the far west Pacific is too far west as shown Fig. 1. The feature also indicates that climatological positions of the ITCZ and the west Pacific convergence centers are all located too far west, because the atmospheric convergence zones always adjust to temperature such that they remain over the areas of warmest surface temperatures. As these convergence zones oscillate from their unrealistic mean locations with ENSO cycles, unrealistic rainfall correlations are generated. A negative correlation over the off-equatorial west Pacific and the northern eastern Indian Ocean in DJF and MAM (Figs. 3e,f) and the unrealistically strong correlation between 150°E and 180° are examples of this bias, as discussed in section 3. Another example is provided in Fig. 15b over west Papua New Guinea in DJF, where there is little ENSO–rainfall teleconnection in the observations but the majority of models generate too strong a teleconnection.

Another consequence of a cold tongue that extends too far west is the ability to distinguish the impacts of traditional ENSO and the so-called ENSO Modoki (Ashok et al. 2007), which has an anomaly center located near the international date line, as opposed to the center near the central eastern Pacific, for example the Niño-3 region (an index of ENSO; 5°S–5°N, 150°–90°W) or Niño-3.4 region. Following Ashok et al. (2007), an El Niño Modoki index (EMI) is constructed for each season, defined as

$$\mathrm{EMI} = [\mathrm{SSTA}]_A - 0.5 \times [(\mathrm{SSTA})_B + (\mathrm{SSTA})_C],$$

where SSTA represents the area-averaged SST anomalies for the regions A (10°S–10°N, 165°E–140°W), B (15°S–5°N, 110°–70°W), and C (10°S–20°N, 125°–145°E). In most models, the date line center is also a part of the

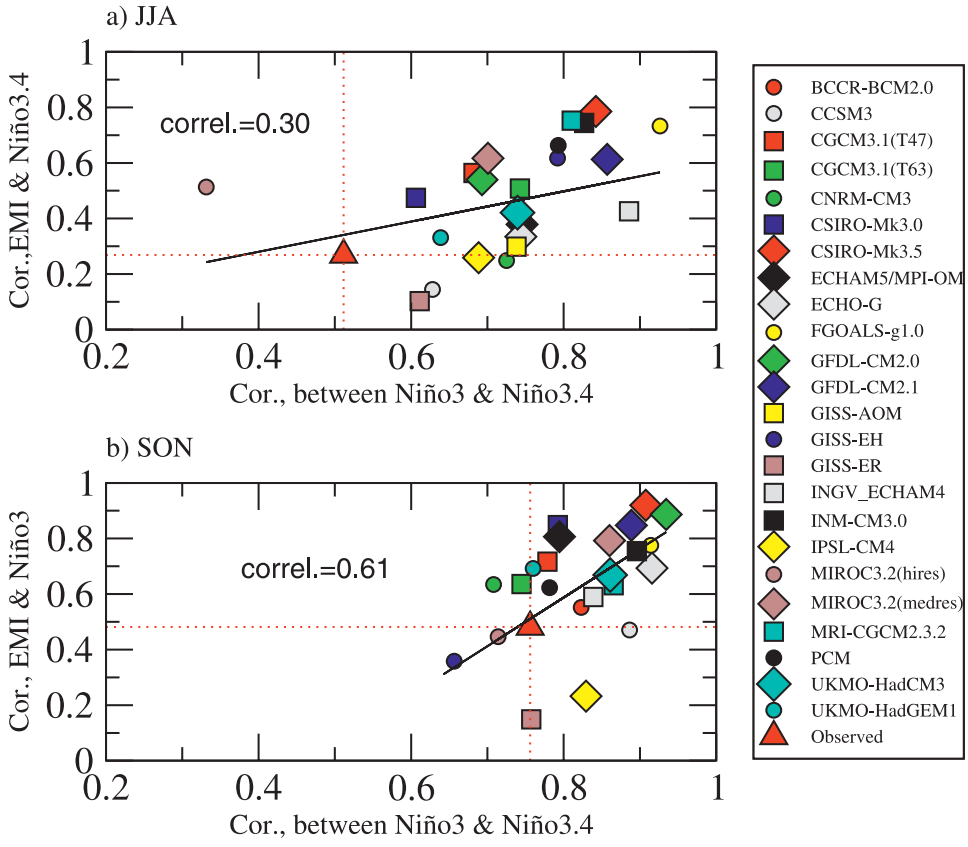

FIG. 16. Scatterplot of intermodel variations of EMI–Niño-3 correlations against intermodel variations of Niño-3.4–Niño-3 correlations for (a) JJA and (b) SON.

model ENSO center, which extends from the Niño-3 region. Figure 16 plots the correlation coefficient between Niño-3 and Niño-3.4 against the correlation between Niño-3 and EMI for JJA and SON. In JJA, ENSO Modoki affects the Indian monsoon (Ashok et al. 2007), and in SON it has a broader impact on Australian rainfall (Wang and Hendon 2007). The majority of the models produce too strong a coherence between the EMI and Niño-3 and between Niño-3 and Niño-3.4, indicating that in most models the ability to simulate the distinction between ENSO Modoki and the traditional ENSO is reduced.

Consequently, there is little difference between the Niño-3–rainfall teleconnection and the EMI–rainfall relationship. Plotted in Fig. 17 are the correlations between Niño-3 and gridpoint Australian rainfall and between EMI and gridpoint Australian rainfall in SON. The modeled impacts are different from those in the observed (Figs. 17a,b), which shows that ENSO Modoki has a broader influence, with a stronger impact in eastern Australia than the traditional ENSO (Wang and Hendon 2007). However, there is little difference between the correlation with Niño-3 and with EMI (Figs. 17c and 17d, respectively) in the all-model average. Thus, the equatorial Pacific SST bias appears to lead to artificially reduced inter–El Niño (or inter–La Niña) differences in the rainfall teleconnection arising from variations in the ENSO anomaly pattern. Thus, in the models, the most important factor controlling the ENSO–rainfall teleconnection is the model ENSO amplitude and its relative strength to noise. In reality, inter–El Niño variations in the ENSO anomaly pattern provide another important factor.

b. Comparisons between IOD–rainfall and ENSO–rainfall teleconnection

As shown in Figs. 3 and 11, SON rainfall over the SEA region is influenced by ENSO and the IOD, with both the ENSO–rainfall and IOD–rainfall teleconnections reasonably simulated. A scatterplot of intermodel variations of these teleconnections reveals a systematic relationship: models with a stronger ENSO–rainfall teleconnection have a stronger IOD–rainfall teleconnection (Fig. 18a). The relationship is statistically significant at the 95% confidence level. Does this imply an overly strong influence by ENSO over the IOD?

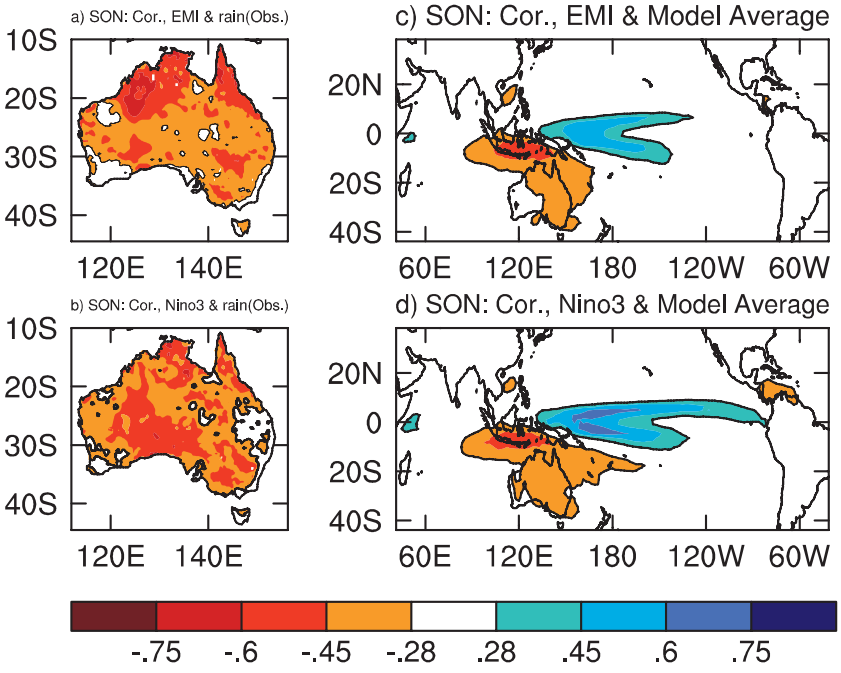

FIG. 17. Correlation between (a) EMI and gridpoint Australian rainfall and (b) between Niño-3 and Australian rainfall for SON; (c),(d) the same as (a) and (b) but averaged over all models.

The answer is negative. An important indication of an ENSO influence on the IOD, or vice versa, is the coherence between them. Using 17 models, Saji et al. (2006) showed that there is no systematic relationship between the IOD and ENSO after the outlier models are removed. Figure 18b plots intermodel variations of the ENSO amplitude against intermodel variations of an ENSO–IOD correlation, that is, between Niño-3.4 and the Indian Ocean SST EOF1 time series. We see that the majority of the models produce a coherence that is lower than the observed. Indeed, after removing an outlier model (FGOALS-g1.0), the relationship, with a correlation of 0.37 (red fitting line in Fig. 18b), is not significant at the 95% confidence level, supporting the finding that, although El Niño is a trigger for the IOD, other causes also operate (Shinoda et al. 2004; Yamagata et al. 2004; Saji et al. 2006). These studies suggest that a Bjerknes feedback between the zonal wind and the thermocline can generate an unstable growth of an initial perturbation regardless of its trigger. Possible triggers may include the southern annular mode (Lau and Nath 2004) and the onset of monsoon (Fischer et al. 2005; Behera et al. 2005). A detailed examination of these causes is beyond the scope of this study.

It follows that the relationship shown in Fig. 18a is a consequence of the feature that models with large amplitudes tend to have large IOD amplitudes as well, each contributing to a large "signal to noise" ratio. The intermodel variations of the model IOD amplitude appears to increase systematically with intermodel variations of the ENSO amplitude (Fig. 18c) with a correlation of 0.65 using all 24 models. For a given model, the strength of Bjerknes feedback and the interactions between wind, SST, and rainfall in the Indian and Pacific Oceans are commensurate once model parameterizations such as atmospheric convection and oceanic mixing are determined. Recent studies examining the simulation of these feedbacks and interactions in the Indian Ocean (Saji et al. 2006) and the Pacific Ocean (van Oldenborgh et al. 2005; Lin 2007) support this notion.

Is there a subgroup of models in which the intermodel variations of the ENSO amplitude control the intermodel variations of ENSO–IOD coherence? If so, it would mean that in this group ENSO is a more important trigger of the IOD than in the rest of models. As discussed by Saji et al. (2006) and Cai et al. (2005), the ENSO–IOD coherence depends on a model's ability to simulate not only the atmospheric but also the oceanic teleconnection between the Indo-Pacific system. The oceanic teleconnection is conducted through the Indonesian Throughflow Passage, whereby ENSO signals transmit to the Indian Ocean arriving at the NWA coast and then radiate into the Indian Ocean interior (Cai et al. 2008). The transmission consists of two pathways: an equatorial Pacific (EP) wave pathway, in which equatorial Rossby waves become coastally trapped waves

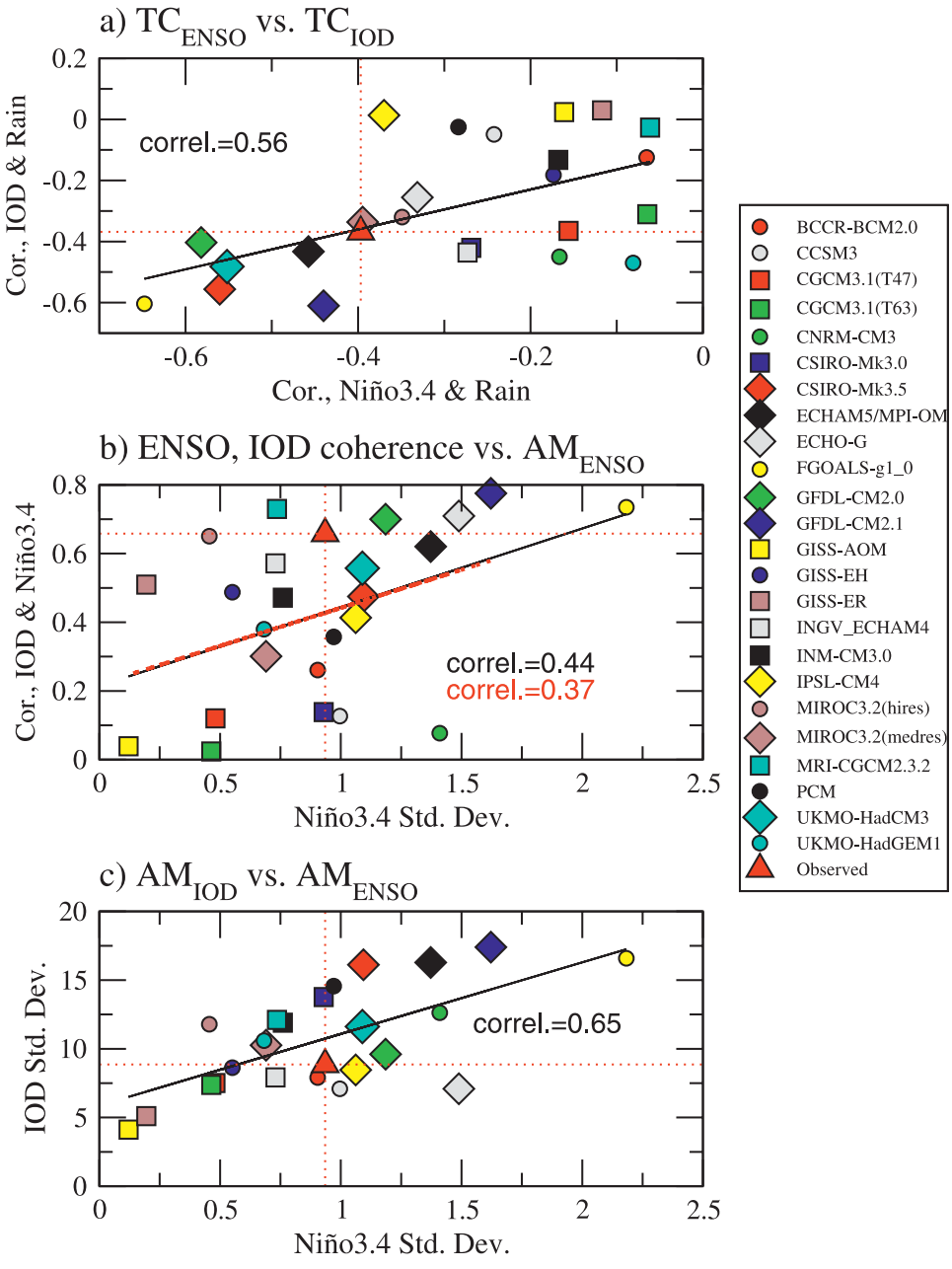

FIG. 18. Scatterplot of (a) intermodel variations of the SON ENSO–rainfall teleconnection against intermodel variations of the SON IOD–rainfall teleconnection, (b) intermodel variations of SON ENSO–IOD coherence against intermodel variations of the SON ENSO amplitude, and (c) intermodel variations of the SON IOD variance against intermodel variations of the SON ENSO amplitude. In (b), an additional regression line (red) is obtained without the outlier model (FGOALS-g1.0).

near where the western New Guinea coast intersects the equator in the west Pacific (Clarke and Liu 1994; Potemra 2001; Wijffels and Meyers 2004), and a subtropical North Pacific (NP) wave pathway (Cai et al. 2005; Shi et al. 2007), in which off-equatorial NP Rossby waves associated with ENSO impinge on the western boundary and move equatorward along the pathway of Kelvin–Munk waves (Godfrey 1975); upon reflecting as equatorial Kelvin waves, these waves converge on the EP pathway. The transmission in each model is examined using lag-correlation analysis between detrended Niño-3.4 and monthly anomalies of upper-250-m ocean heat content. The transmission in each model is then observed. ENSO signals at NWA usually reach a maximum

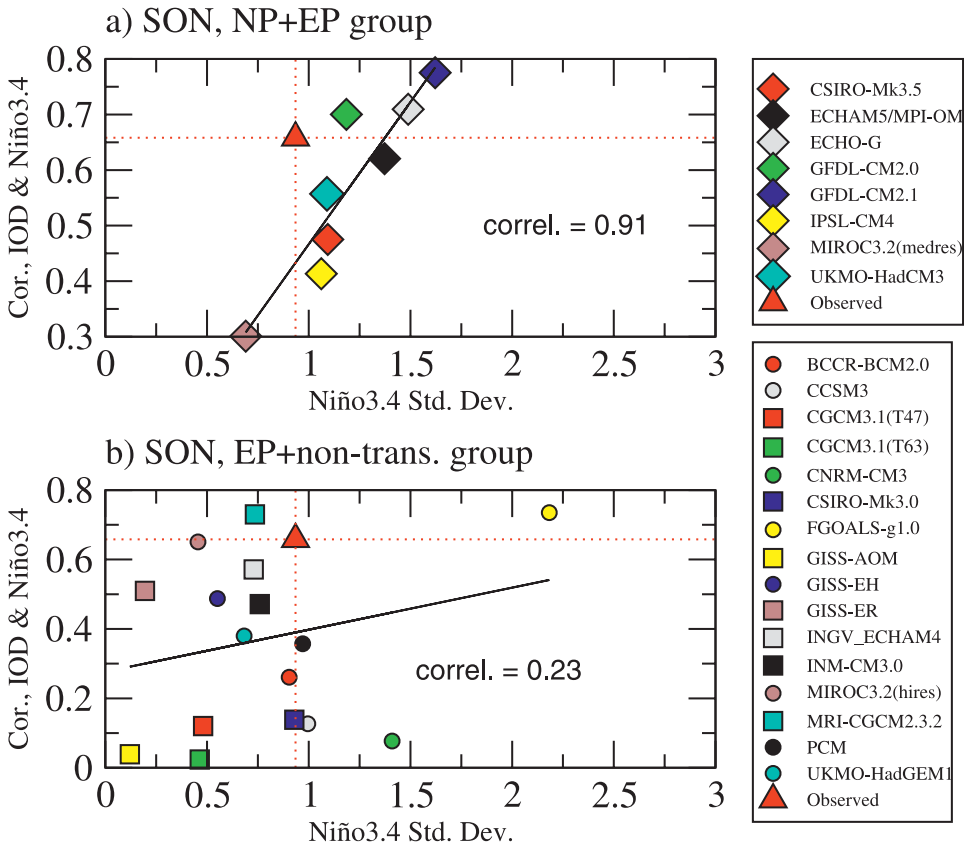

FIG. 19. Scatterplot of intermodel variations of SON ENSO–IOD coherence against intermodel variations of the SON ENSO amplitude (a) using models which more realistically simulate the ENSO anomaly pattern, ENSO amplitude, and ENSO transmission signals to the Indian Ocean and (b) using the remaining models.

3–6 months after the mature phase of ENSO. Throughout this paper, we have used three different shapes to denote models (Fig. 18). The 8 models indicated by diamonds are those with transmission via both pathways (NP + EP), the 8 models shown as circles transmit via the EP pathway only, and the remaining 8 models are shown as squares with no transmission or incorrect transmission pathways.

In the NP + EP group, the relationship between intermodel variations of the ENSO amplitude and the intermodel variations of the ENSO–IOD coherence is significant at the 95% confidence level (an absolute value of 0.71 is required for 8 models; Fig. 19a). There is no significant relationship between the ENSO–IOD coherence and ENSO amplitude once models in the NP + EP group are excluded (Fig. 19b), suggesting that IOD events within the remaining models are more likely to be triggered by drivers beyond ENSO. The involvement of the NP pathway is an indication of a model ENSO anomaly pattern that has a broader meridional extent (Fig. 20a) than that in, for example, the EP group (Fig. 20d). The associated broader ENSO wind anomalies in the NP + EP group (Fig. 20b) than the EP group (Fig. 20e) are able to force NP off-equatorial Rossby waves. Furthermore, the broader meridional extent in the NP + EP group is accompanied by generally stronger ENSO amplitudes and hence stronger wind anomalies over the eastern Indian Ocean, which enhances the ENSO–IOD coherence through the Bjerknes positive feedback involving the wind, thermocline, and SST. This is indicated by a stronger ENSO heat content signal-to-noise ratio in the NP + EP group (Fig. 20c), as opposed to the EP-only group (Fig. 20f) in which the overall more realistic pattern and stronger ENSO signals are shown. It is these models in the NP + EP group that contribute to the relationship of a stronger IOD–rainfall teleconnection associated with a stronger ENSO–rainfall teleconnection in SON (Fig. 18a) in which both IOD and ENSO have a significant impact.

It is worth noting that even models in the NP + EP group produce on average an ENSO–IOD coherence that is weaker than the observed. This weak coherence

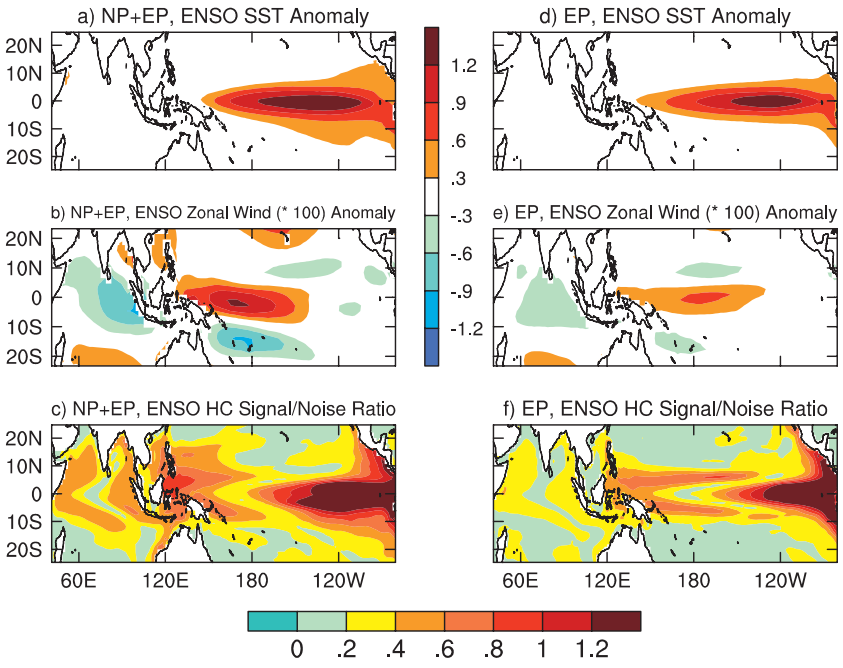

FIG. 20. One standard deviation anomaly pattern associated with Niño-3.4 averaged over the eight models with signals arriving at NWA coast through the EP and NP pathways: (a) SST, (b) zonal wind, and (c) upper-250-m heat content signal-to-noise ratio. (d)–(f) The same as (a)–(c) but for the eight models with signal transmission to the NWA coast through the EP pathway only.

would mean that the superimposing impact of the IOD and ENSO may be underestimated.

6. Conclusions

In recent years, significant improvements in the simulation of ENSO and the IOD in terms of amplitude and frequencies have been achieved. These modes of the Indo-Pacific variability affect global rainfall, particularly throughout the tropical latitudes. Given that climate change and subsequent impacts tend to manifest through existing modes of variability, future rainfall changes rely heavily on the ability of climate models to simulate the strength and spatial pattern of rainfall teleconnections. An assessment of model performance in this respect and identifying associated deficiencies is therefore important for reducing uncertainty in climate change projections.

We show that the strength of a teleconnection for a given location is overwhelmingly controlled by the amplitude of ENSO, and even more strongly by its signal strength relative to stochastic noise, highlighting the importance of realistically simulating these parameters. The deficiencies in the spatial pattern of the ENSO–rainfall teleconnection are mostly attributable to errors in the climatological SST and ENSO SST anomaly pattern. The ENSO–rainfall teleconnection mainly arises from the movement of convergence zones from their mean positions. The well-known equatorial Pacific SST climatology and ENSO cold tongue anomaly biases lead to many systematic errors. For example, the climatologically cold equatorial SSTs lead to a complete ''nonresponse'' in terms of ENSO along the central and eastern equatorial Pacific in many models, the feature of ENSO anomalies being too equatorially confined is linked to a teleconnection that is too weak with Hawaii boreal winter rainfall, and the feature of ENSO anomalies extending too far west induces a teleconnection with rainfall over west Papua New Guinea in austral summer. Another consequence of the El Niño cold tongue extension is that the majority of models produce too strong a coherence between SST anomalies in the west, central, and east equatorial Pacific and fail to reproduce differences in the impacts of ENSO from those of the so-called ENSO Modoki.

Similarly, the IOD–rainfall teleconnection strengthens with the amplitude of the IOD and its relative strength to that of noise. The relationship between the ENSO–rainfall teleconnection and the IOD–rainfall teleconnection is addressed. In general, there is no systematic linkage between the ENSO amplitude and IOD–ENSO coherence. Indeed, the majority of models produce an ENSO–IOD relationship lower than the observed,

supporting the notion that the Indian Ocean has variability beyond ENSO and that ENSO is not the only trigger of IOD events. A subset of models, which are more realistic in terms of ENSO structure and amplitude, and its oceanic teleconnection with the Indian Ocean still produce a weaker ENSO–IOD coherence than the observed. Although the IOD and subsequent rainfall teleconnection appear to increase with the ENSO amplitude, there is generally no causal relationship; instead, they are a consequence of the Pacific and the Indian Ocean having a comparable strength of the Walker circulation.

There are several important issues that need to be explored. Given the importance of the signal-to-noise ratio to the simulation of a rainfall teleconnection, and given the fact that climate change signals tend to project onto modes of variability, will future rainfall changes vary with the signal-to-noise ratio of climate drivers in the present-day climate? Furthermore, how do future rainfall changes depend on a realistic simulation of the level of coherence between the major climate drivers? These will be pursued in a separate study.

Acknowledgments. The authors are supported in part by the Department of Climate Change and in part by the Queensland Urban Water Security Alliance. We thank the two anonymous reviewers and the Chief Editor for their helpful comments. In addition, we acknowledge the outstanding work undertaken by the many international modeling groups who provided their numerous model experiments for the Program for Climate Model Diagnosis and Intercomparison (PCMDI). For more details on model data or documentation, readers are referred to the PCMDI Web site (http://www-pcmdi.llnl.gov).

REFERENCES

AchutaRao, K., and K. Sperber, 2002: Simulation of the El Niño Southern Oscillation: Results from the Coupled Model Intercomparison Project. *Climate Dyn.,* **19,** 191–209.

Alexander, M. A., I. Bladé, M. Newman, J. R. Lazante, N.-C. Lau, and J. D. Scott, 2002: The atmospheric bridge: The influence of ENSO teleconnections on air–sea interaction over the global oceans. *J. Climate,* **15,** 2205–2231.

Annamalai, H., K. Hamilton, and K. R. Sperber, 2007: The South Asian summer monsoon and its relationship with ENSO in the IPCC AR4 simulations. *J. Climate,* **20,** 1071–1092.

Ashok, K., Z. Guan, and T. Yamagata, 2001: Impact of the Indian Ocean dipole on the relationship between the Indian monsoon rainfall and ENSO. *Geophys. Res. Lett.,* **28** (23), 4499–4502.

——, ——, and ——, 2003: Influence of the Indian Ocean Dipole on the Australian winter rainfall. *Geophys. Res. Lett.,* **30,** 1821, doi:10.1029/2003GL017926.

——, S. K. Behera, S. A. Rao, H. Weng, and T. Yamagata, 2007: El Niño Modoki and its possible teleconnection. *J. Geophys. Res.,* **112,** C11007, doi:10.1029/2006JC003798.

Ashrit, R. G., H. Douville, and K. Rupakumar, 2003: Response of Indian monsoon and ENSO-monsoon teleconnection to enhanced greenhouse effect in the CNRM coupled model. *J. Meteor. Soc. Japan,* **81,** 779–803.

Behera, S. K., J. J. Luo, S. Masson, P. Delecluse, S. Gualdi, and A. Navarra, 2005: Paramount impact of the Indian Ocean dipole on the East African short rains: A CGCM study. *J. Climate,* **18,** 4514–4530.

Black, E., J. Slingo, and K. R. Sperber, 2003: An observational study of the relationship between excessively strong short rains in coastal East Africa and Indian Ocean SST. *Mon. Wea. Rev.,* **131,** 74–94.

Cai, W., and P. H. Whetton, 2001: A time-varying greenhouse warming pattern and the tropical–extratropical circulation linkage in the Pacific Ocean. *J. Climate,* **14,** 3337–3355.

——, and T. Cowan, 2006: The SAM and regional rainfall in IPCC AR4 models: Can anthropogenic forcing account for southwest Western Australian rainfall reduction. *Geophys. Res. Lett.,* **33,** L24708, doi:10.1029/2006GL028037.

——, M. A. Collier, H. B. Gordon, and L. J. Waterman, 2003: Strong ENSO variability and a super-ENSO pair in the CSIRO Mark 3 coupled climate model. *Mon. Wea. Rev.,* **131,** 1189–1210.

——, H. H. Hendon, and G. Meyers, 2005: Indian Ocean dipole-like variability in the CSIRO Mark 3 coupled climate model. *J. Climate,* **18,** 1449–1468.

——, A. Sullivan, and T. Cowan, 2008: Shoaling of the off-equatorial south Indian Ocean thermocline: Is it driven by anthropogenic forcing? *Geophys. Res. Lett.,* **35,** L12711, doi:10.1029/2008GL034174.

Clarke, A. J., and X. Liu, 1994: Interannual sea level in the northern and eastern Indian Ocean. *J. Phys. Oceanogr.,* **24,** 1224–1235.

Collins, M., 2005: El Niño- or La Niña-like climate change? *Climate Dyn.,* **24,** 89–104.

Davey, M. K., and Coauthors, 2002: STOIC: A study of coupled model climatology and variability in tropical ocean regions. *Climate Dyn.,* **18,** 403–420.

Fischer, A., P. Terray, E. Guilyardi, S. Gualdi, and P. Delecluse, 2005: Two independent triggers for the Indian Ocean dipole zonal mode in a coupled GCM. *J. Climate,* **18,** 3428–3449.

Godfrey, J. S., 1975: On ocean spindown I: A linear experiment. *J. Phys. Oceanogr.,* **5,** 399–409.

Guilyardi, E., 2006: El Niño–mean state–seasonal cycle interactions in a multi-model ensemble. *Climate Dyn.,* **26,** 329–348, doi:10.1007/s00382-005-0084-6.

Joseph, R., and S. Nigam, 2006: ENSO evolution and teleconnection in IPCC's twentieth-century climate simulations: Realistic representation? *J. Climate,* **19,** 4360–4377.

Kalnay, E., and Coauthors, 1996: The NCEP/NCAR 40-Year Reanalysis Project. *Bull. Amer. Meteor. Soc.,* **77,** 437–471.

Klein, S. A., B. J. Soden, and N. C. Lau, 1999: Remote sea surface temperature variations during ENSO: Evidence for a tropical atmospheric bridge. *J. Climate,* **12,** 917–932.

Latif, M., and Coauthors, 2001: ENSIP: The El Niño simulation intercomparison project. *Climate Dyn.,* **18,** 255–276.

Lau, N.-C., and M. J. Nath, 2004: Coupled GCM simulation of atmosphere–ocean variability associated with the zonally asymmetric SST changes in the tropical Indian Ocean. *J. Climate,* **17,** 245–265.

Lin, J. L., 2007: The double-ITCZ problem in IPCC AR4 coupled GCMs: Ocean–atmosphere feedback analysis. *J. Climate,* **20,** 4497–4525.

Liu, Z., and M. Alexander, 2007: Atmospheric bridge, oceanic tunnel, and global climatic teleconnections. *Rev. Geophys.,* **45,** RG2005, doi:10.1029/2005RG000172.

Lu, J., G. Chen, and D. Frierson, 2008: Response of the zonal mean atmospheric circulation to El Niño versus global warming. *J. Climate,* **21,** 5835–5851.

McBride, J. L., and N. Nicholls, 1983: Seasonal relationships between Australian rainfall and the Southern Oscillation. *Mon. Wea. Rev.,* **111,** 1998–2004.

Mechoso, C. R., and Coauthors, 1995: The seasonal cycle over the tropical Pacific in coupled ocean–atmosphere general circulation models. *Mon. Wea. Rev.,* **123,** 2825–2838.

Meehl, G. A., and W. M. Washington, 1996: El Niño-like climate change in a model with increased atmospheric CO2 concentration. *Nature,* **382,** 56–60.

——, C. Covey, B. McAvaney, M. Latif, and R. J. Stouffer, 2005: Overview of the Coupled Model Intercomparison Project. *Bull. Amer. Meteor. Soc.,* **86,** 89–93.

Murtugudde, R. G., J. P. McCreary, and A. J. Busalacchi, 2000: Oceanic processes associated with anomalous events in the Indian Ocean with relevance to 1997–1998. *J. Geophys. Res.,* **105,** 3295–3306.

Philander, S. G. H., 1990: *El Niño, La Niña, and the Southern Oscillation*. Academic Press, 289 pp.

Potemra, J. T., 2001: The potential role of equatorial Pacific winds on southern tropical Indian Ocean Rossby waves. *J. Geophys. Res.,* **106,** 2407–2422.

Rayner, N. A., D. E. Parker, E. B. Horton, C. K. Folland, L. V. Alexander, D. P. Rowell, E. C. Kent, and A. Kaplan, 2003: Global analyses of sea surface temperature, sea ice, and night marine air temperature since the late nineteenth century. *J. Geophys. Res.,* **108,** 4407, doi:10.1029/2002JD002670.

Ropelewski, C. F., and M. S. Halpert, 1987: Global and regional scale precipitation patterns associated with the El Niño/Southern Oscillation. *Mon. Wea. Rev.,* **115,** 1606–1626.

——, and ——, 1989: Precipitation patterns associated with high index phase of Southern Oscillation. *J. Climate,* **2,** 268–284.

Saji, N. H., and T. Yamagata, 2003a: Possible impacts of Indian Ocean dipole mode events on global climate. *Climate Res.,* **25,** 151–169.

——, and ——, 2003b: Structure of SST and surface wind variability during Indian Ocean dipole mode years: COADS observations. *J. Climate,* **16,** 2735–2751.

——, B. N. Goswami, P. N. Vinayachandran, and T. Yamagata, 1999: A dipole mode in the tropical Indian Ocean. *Nature,* **401,** 360–363.

——, S.-P. Xie, and T. Yamagata, 2006: Tropical Indian Ocean variability in the IPCC twentieth-century climate simulations. *J. Climate,* **19,** 4397–4417.

Scaife, A., and Coauthors, 2008: The CLIVAR C20C Project: Selected twentieth century climate events. *Climate Dyn.,* **31,** doi:10.1007/s00382-008-0451-1.

Shi, G., J. Ribbe, W. Cai, and T. Cowan, 2007: Multidecadal variability in the transmission of ENSO signals to the Indian Ocean. *Geophys. Res. Lett.,* **34,** L09706, doi:10.1029/2007GL029528.

——, W. Cai, T. Cowan, J. Ribbe, L. Rotstayn, and M. Dix, 2008a: Variability and trend of the northwest Western Australia rainfall: Observations and coupled climate modeling. *J. Climate,* **21,** 2938–2959.

——, J. Ribbe, W. Cai, and T. Cowan, 2008b: An interpretation of Australian rainfall projections. *Geophys. Res. Lett.,* **35,** L02702, doi:10.1029/2007GL032436.

Shinoda, T., H. H. Hendon, and M. A. Alexander, 2004: Surface and subsurface dipole variability in the Indian Ocean and its relation with ENSO. *Deep-Sea Res.,* **51,** 619–635.

Shukla, J., and D. A. Paolino, 1983: The Southern Oscillation and long-range forecasting of summer monsoon rainfall over India. *Mon. Wea. Rev.,* **111,** 1830–1837.

Timmermann, A. J., J. Oberhuber, A. Bacher, M. Esch, M. Latif, and E. Roeckner, 1999: Increased El Niño frequency in a climate model forced by future greenhouse warming. *Nature,* **398,** 694–697.

Turner, A. G., P. M. Inness, and J. M. Slingo, 2005: The role of the basic state in the ENSO-monsoon relationship and implications for predictability. *Quart. J. Roy. Meteor. Soc.,* **131,** 781–804.

van Loon, H., and D. Shea, 1985: The Southern Oscillation. Part IV: The precursors south of 15°S to the extremes of the oscillation. *Mon. Wea. Rev.,* **113,** 2063–2074.

van Oldenborgh, G. J., S. Y. Philip, and M. Collins, 2005: El Niño in a changing climate: A multi-model study. *Ocean Sci.,* **1,** 81–95.

Vecchi, G. A., B. J. Soden, A. T. Wittenberg, I. M. Held, A. Leetmaa, and M. J. Harrison, 2006: Weakening of tropical Pacific atmospheric circulation due to anthropogenic forcing. *Nature,* **441,** 73–76, doi:10.1038/nature04744.

Wang, G., and H. Hendon, 2007: Sensitivity of Australian rainfall to inter–El Niño variations. *J. Climate,* **20,** 4211–4226.

Webster, P. J., A. M. Moore, J. P. Loschnigg, and R. R. Leben, 1999: Coupled ocean–atmosphere dynamics in the Indian Ocean during 1997–98. *Nature,* **401,** 356–360.

Wijffels, S., and G. Meyers, 2004: An intersection of oceanic waveguides: Variability in the Indonesian Throughflow region. *J. Phys. Oceanogr.,* **34,** 1232–1253.

Xie, P., and P. A. Arkin, 1997: Global precipitation: A 17-year monthly analysis based on gauge observations, satellite estimates, and numerical model outputs. *Bull. Amer. Meteor. Soc.,* **78,** 2539–2558.

Xie, S.-P., H. Annamalai, F. A. Schott, and J. P. McCreary, 2002: Structure and mechanisms of south Indian Ocean climate variability. *J. Climate,* **15,** 864–878.

Yamagata, T., S. K. Behera, J. J. Luo, S. Masson, M. R. Jury, and S. A. Rao, 2004: Coupled ocean–atmosphere variability in the tropical Indian Ocean. *Earth Climate: The Ocean–Atmosphere Interaction, Geophys. Monogr.,* Vol. 147, Amer. Geophys. Union, 189–212.

Yulaeva, E., and J. M. Wallace, 1994: The signature of ENSO in global temperature and precipitation fields derived from the microwave sounding unit. *J. Climate,* **7,** 1719–1736.

Zubair, L., S. A. Rao, and T. Yamagata, 2003: Modulation of Sri Lankan *Maha* rainfall by the Indian Ocean dipole. *Geophys. Res. Lett.,* **30,** 1063, doi:10.1029/2002GL015639.